LAWRENCE
LIVERMORE
NATIONAL
LABORATORY

UCRL-JRNL-205588

The Madden-Julian Oscillation in the National Center for Atmospheric Research Community Atmospheric Model-2 with the Tiedtke Convective Scheme

P. Liu, B. Wang, K. R. Sperber,
T. Li, and G. A. Meehl

July 29, 2004

Journal of Climate

Disclaimer

This document was prepared as an account of work sponsored by an agency of the United States Government. Neither the United States Government nor the University of California nor any of their employees, makes any warranty, express or implied, or assumes any legal liability or responsibility for the accuracy, completeness, or usefulness of any information, apparatus, product, or process disclosed, or represents that its use would not infringe privately owned rights. Reference herein to any specific commercial product, process, or service by trade name, trademark, manufacturer, or otherwise, does not necessarily constitute or imply its endorsement, recommendation, or favoring by the United States Government or the University of California. The views and opinions of authors expressed herein do not necessarily state or reflect those of the United States Government or the University of California, and shall not be used for advertising or product endorsement purposes.

The Madden-Julian Oscillation in the National Center for Atmospheric Research Community Atmospheric Model-2 with the Tiedtke Convective Scheme

Ping Liu, Bin Wang
International Pacific Research Center, University of Hawaii,
1680 East-West Road, Honolulu, HI 96822
Kenneth R. Sperber
PCMDI, P.O. Box 808, L-103, Livermore, CA 94551-0808
Tim Li
International Pacific Research Center, University of Hawaii,
1680 East-West Road, Honolulu, HI 96822
Gerald A. Meehl
National Center for Atmospheric Research, 1850 Table Mesa DR., Boulder, CO 80305

Abstract

The boreal winter Madden-Julian oscillation (MJO) remains very weak and irregular in structure in the National Center for Atmospheric Research (NCAR) Community Atmosphere Model version 2 (CAM2) as in its direct predecessor, the Community Climate Model version 3 (CCM3). The standard version of CAM2 uses the deep convective scheme of Zhang and McFarlane (1995), as in CCM3, with the closure dependent on convective available potential energy (CAPE). Here, sensitivity tests using several versions of the Tiedtke (1989) convective scheme are conducted. Typically, the Tiedtke convection scheme gives an improved mean state, intraseasonal variability, space-time power spectra, and eastward propagation compared to the standard version of the model. Coherent eastward propagation of MJO related precipitation is also much improved, particularly over the Indian-western Pacific Oceans. Sensitivity experiments show that enhanced downdrafts in the Tiedtke scheme reduces the amplitude of the MJO but to a lesser extent than when this scheme is closed on CAPE to represent deep convections. A composite life cycle of the model MJO indicates that over the Indian Ocean wind induced surface heat exchange functions, while over the western/central Pacific Ocean aspects of frictional moisture convergence are evident in the maintenance and eastward propagation of the oscillation.

1. Introduction

The Madden-Julian oscillation (MJO), first discovered by Madden and Julian (1971; 1972), is the dominant mode of intraseasonal variability and considered to play an important role in time and space scale interactions in the climate system (Meehl et al. 2001). Characteristic features of the MJO include power spectra dominated by periods of 30-70 days and zonal wave numbers 1-3, overwhelmingly stronger eastward than westward propagation, out-of-phase structure of 850 and

200 hPa wind, higher amplitude during boreal winter than summer, and coherent propagation among convective and dynamical fields (Madden and Julian 1994; Hendon and Salby 1994). A mixed Kelvin-Rossby wave structure is characteristic over the Indian and western Pacific Oceans, where the circulation is strongly coupled to convection and propagates slowly eastward as a set of super cloud clusters (e.g. Rui and Wang 1990; Chao and Lin 1994). The oscillation has a Kelvin wave structure with more rapid eastward propagation in regions away from the main convection.

Evolution and eastward propagation of the MJO involve complicated interactions among large-scale circulations, tropical planetary waves, boundary layer moisture supply, transport and phase change of water vapor and the associated latent heat release (Meehl et al. 1996). Several modeling studies (e.g., Wang 1988; Wang and Rui 1990; Salby et al. 1994; Seager and Zebiak 1994; Wang and Li 1994; Waliser et al. 1999; Maloney and Hartmann 2001; Maloney 2002) suggest that frictional convergence in the boundary layer east of the main convective area is of great importance to the evolution and eastward propagation of the MJO. Convection is enhanced above boundary convergence, while it is suppressed by boundary divergence. Observational investigations (Hendon and Salby 1994; Salby and Hendon 1994; Jones and Weare 1996; Maloney and Hartmann 1998, MH98 in short; Woolnough et al 2000; Sperber 2003) also support that low-level moisture convergence occurs to the east of the main convective area associated with the MJO.

Many studies (Hendon and Liebmann 1990; Blade and Hartmann 1993; Hu and Randall 1994; MH98; Maloney and Hartmann 2001) suggest that the atmosphere should be preconditioned before being able to sustain deep convection associated with the MJO. The lower troposphere moistens slowly and goes through a period of buildup of moist static energy before deep convection onsets. The atmosphere then dries quickly as the convection commences and anomalous westerly winds ensue (Blade and Hartmann 1993). MH98 further validated that a period of build-up of moisture is required over the Indian and west Pacific Oceans before significant convection can occur, and that it in fact sets the timescale of the transition in convection from the Indian Ocean to the west Pacific Ocean. Frictional surface convergence is a key factor in this preconditioning of the atmosphere.

Global atmospheric general circulation models (AGCMs) have a wide range of ability in simulating the observed MJO features (Park et al. 1990; Slingo et al. 1996; Maloney and Hartmann 2001). Many models can reproduce stronger eastward than westward propagating equatorial zonal wind signals but coherent propagation of convection is less well simulated. Most AGCMs analyzed by Park et al. (1990) and Slingo et al. (1996) produce MJO-like signals with higher than observed phase speeds in convective regions, periods that are too fast (<30 days), and with an amplitude smaller than observed. Little apparent seasonality of the MJO signals exists in those models. Slingo et al. (1996) further suggested AGCMs that have a better mean state tend to produce a more realistic MJO. Recent modeling studies of MJO using coupled GCMs have demonstrated that realistic simulation of the mean state in the coupled model is even more critical (Gualdi et al. 1999; Hendon 2000). Kemball-Cook et al. (2002) found that their coupled model failed in simulating August-October MJO in the western North Pacific because the mean SST in the coupled model was too cold and the monsoonal mean vertical easterly shears

were absent. The mean surface westerlies in the western Pacific was found of critical importance for winter MJO simulation (Hendon 2000; Inness and Slingo 2003; Inness et al. 2003).

Convective parameterization schemes implemented in an AGCM play a key role in simulating a reasonable MJO (Inness and Gregory 1997; Wang and Schlesinger 1999; Maloney and Hartmann 2001). Based on comparison of various cumulus parameterization schemes in *different* models, Slingo et al. (1996) suggested that convective schemes closed on buoyancy tend to produce better MJO signals than those closed on moisture convergence. In order to better evaluate the sensitivity of MJO simulations to various cumulus parameterization schemes, a number of recent studies have used a *single* model with differing cumulus schemes (Chao and Deng 1998; Wang and Schlesinger 1999; Maloney and Hartmann 2001; Lee et al. 2003). Both Chao and Deng (1998) and Lee et al. (2003) compared three different schemes, the moist convective adjustment (MCA; Manabe et al. 1965), the Kuo (1974) scheme, and the modified Arakawa-Schubert (1974; AS) scheme. Both studies found that MCA produces the strongest MJO variability while AS scheme the smallest. What causes this sensitivity, however, deserves further investigation. Wang and Schlesinger (1999) also used a single model (the University of Illinois AGCM) with MCA, Kuo, and relaxed AS to simulate MJO. For each parameterization a relative humidity criterion (RHc) for convection or convective heating to occur was used. They found that as RHc increases, the simulated MJO becomes stronger for all three parameterizations. They suggested that when large values of RHc were used, the triggering convection required the moist static energy in the lower troposphere to be accumulated to a certain amount through moisture convergence; this elevated RHc weakened the interaction between the circulation and heating for small-scale perturbations and allowed the MJO to occur at low frequencies. On the other hand, Maloney and Hartmann (2001) found that the MJO in the National Center for Atmospheric Research (NCAR) Community Climate Model, version 3.6 (CCM3) with the relaxed AS scheme is not improved by increasing the RHc. They suggested that the MJO is highly sensitive to the parameterization of the evaporation of convective precipitation in unsaturated environmental air and saturated downdrafts. These diverse results suggest that further study of the sensitivity of the MJO simulation to the closure assumptions in different models and understand where the sensitivity comes from is necessary.

Maloney and Hartmann (2001) showed that the standard CCM3 employing the deep convection parameterization of Zhang and McFarlane (1995) produced the MJO in zonal winds and precipitation with amplitude much weaker than observed. Sheng (1995) showed that there was a weak MJO in the Canadian Climate Center GCM with the same deep convective scheme. Maloney and Hartmann (2001) and Maloney (2002) showed that the MJO was markedly improved by implementing the relaxed Arakawa-Schubert (McRAS) scheme of Moorthi and Suarez (1992) modified by Sud and Walker (1999) to the CCM3. Intraseasonal zonal wind variability was much enhanced with realistic eastward phase speeds. Coherent precipitation variability was also much improved, particularly over the western Pacific warm pool. Sensitivity experiments (Maloney 2002) showed that the wind-induced surface heat exchange (WISHE) mechanism could not explain the coincidence of convection with 850 hPa easterly anomalies. Removing WISHE even produced a more robust MJO. However, as shown by Maloney and Hartmann (2001) and Maloney (2002), the CCM3 with McRAS had some deficiencies especially over the Indian Ocean

where the simulation of convection and wind anomalies was notably weaker than observed. Although the frictional moisture convergence mechanism was present, precipitation was in phase with low-level convergence, different from the quadrature relationship observed.

The fifth generation of the NCAR AGCM, newly named as the Community Atmosphere Model, version 2 (CAM2), is a descendent of the CCM3. Configurations and major changes in the CAM2 from the CCM3 are listed in an overview in section 2. It is noteworthy here that the CAM2 retains the Zhang and McFarlane (1995) scheme for parameterization of deep convection. Consistent with the analysis of Sperber (2004) we will show that this model does not represent the MJO. Similar to the CCM3 (Maloney and Hartmann 2001), the power spectrum of 850 hPa zonal wind in the CAM2 has much lower amplitude than that in observations, with little or no propagating intraseasonal convection.

The intent of this study is to 1) improve the MJO simulation in the CAM2 by implementing the Tiedtke (1989) convective scheme that is closed on moisture convergence, 2) test the sensitivity of the MJO simulation by using the CAPE closure of Nordeng (1994) for deep convections in the Tiedtke (1989) scheme, 3) ascertain the influence of enhanced downdrafts in the simulation of the MJO, and 4) assess the WISHE and frictional moisture convergence mechanisms in a life cycle of the model MJO. MJO in the extended winter season from November to April will be analyzed. Table 1 lists the convective schemes, their closures and downdraft characteristics for the various sensitivity tests.

Section 2 introduces the CAM2, provides an overview of the Tiedtke (1989) scheme and its revised version by Nordeng (1994), and describes observational data, experimental design and procedure for data analysis. Section 3 presents the simulated mean states, MJO features shown in intraseasonal variance, power spectra in zonal wind and precipitation, and regression of 850 hPa zonal winds. Section 4 gives a composite life cycle of the model MJO displaying the function of frictional moisture convergence. Section 5 presents experiments concerning the sensitivity of MJO to enhanced downdrafts and perpetual run design. Section 6 summarizes the results and gives discussions.

2. Model, convective schemes, integrations and observational data

2.1. The NCAR CAM2

In the present study, we use the CAM2.0.2 version released in July 2003. Only small revisions have been made in this latest version compared to the earliest release of CAM2. A horizontal resolution at T42 (approximately 2.8^o longitude by 2.8^o latitude) is specified along with 26 hybrid vertical layers (higher than the 19 vertical layers in the CCM3). We list here an overview of the changes since the CCM3. For a complete document of this model version, readers are referred to the description of the NCAR Community Atmospheric Model version 2 (CAM2) that is available from http://www.ccsm.ucar.edu/models/atm-cam/docs/description/index.html.

The CAM2 has a few major changes in the physical processes. A new prognostic

parameterization of the cloud condensed water treats 1) a macroscale process that describes the exchange of water substance between the condensate and the vapor phase and the associated temperature change arising from that phase change (Zhang et al. 2003); and 2) a bulk microphysical process that controls the conversion from condensate to precipitate (Rasch and Kristjansson 1998). Over the sea ice, a new thermodynamic package is formulated computing snow depth, brine pockets, internal shortwave radiative transfer, surface albedo, ice-atmosphere drag, and surface exchange fluxes. The fractional land and sea-ice coverage is explicitly represented to more accurately define the flux exchanges from coastal boundaries, island regions, and ice edges than the CCM series in which only a simple land-ocean-sea ice mask is used for such definitions. In the radiation calculations, geometrical cloud overlap is treated by a new, general, and flexible parameterization that computes the shortwave and longwave fluxes and heating rates for random overlap, maximum overlap, or an arbitrary combination of maximum and random overlap. Adjacent cloud layers are maximally overlapped and groups of clouds separated by cloud-free layers are randomly overlapped. The introduction of the generalized overlap assumptions permits more realistic treatments of cloud-radiative interactions. A new parameterization, the General Line-by-line Atmospheric Transmittance and Radiance Model (GENLN2), is employed for the longwave absorptivity and emissivity of water vapor treatment. The Zhang and McFarlane (1995) scheme for deep convection and Hack (1994) scheme for shallow and mid-level convection are retained. We will show later that these convective schemes retain the unrealistic simulation of the MJO in the CAM2. Evaporation of convective precipitation following Sundqvist (1988) is incorporated and can enhance the atmospheric moisture and offset the drying introduced by changes in the longwave absorptivity and emissivity.

2.2. Convective schemes

We ported the convective parameterization scheme of Tiedtke (1989), revised by Nordeng (1994) from the ECHAM (Roeckner et al. 1996) AGCM version 4 developed at the Max Planck Institute for Meteorology to the CAM2. The scheme and its revised versions are briefly summarized here, showing the primary differences from that of Zhang and McFarlane (1995). Details of the alternative convection schemes can be found in Tiedtke (1989) and Nordeng (1994). See Table 1 for a synopsis of the schemes employed in the various sensitivity experiments.

The Tiedtke (1989) convective parameterization is based on the mass flux concept. This scheme considers deep, shallow and mid-level convection. Only one type of convection is allowed to take place each time when the scheme is activated. An ensemble of clouds occurring in each type of convection is assumed to consist of updrafts and downdrafts. The cumulative effect of these clouds contributes to large-scale general circulation, functioning as a bulk model. Updrafts usually have entrainment and detrainment from boundary layer turbulence and organized large-scale advection starting from cloud base at the level of free lifting. Downdrafts occur at the level of free sinking (LFS) where in-cloud air mixes with out-cloud (or environmental) air and becomes unstable relative to the environment. Mass flux at LFS is taken as a fraction of the cloud base mass flux, 20% being assumed in Tiedtke (1989). Moisture convergence is used to determine cloud base mass flux and close the scheme. When the convergence is greater than a limit of boundary layer turbulent moisture flux, convection is activated. Deep or penetrative

convection takes place when column integrated moisture convergence exceeds a prescribed percentage of boundary layer turbulent moisture flux (110% is assumed as in the ECHAM4). The simulated mean state and MJO are not sensitive to this limit unless it is specified far beyond the value currently used. Shallow convection occurs in a suppressed environment where there is surface turbulent moisture flux and large-scale moisture can be small or even negative. Large-scale lifting of potentially unstable upper air activates mid-level convection. In the ECHAM4, 30% of cloud base mass flux is assumed to be downdrafts. Previous studies (e.g. Maloney and Hartmann 2001) have shown that the downdrafts are important to the MJO simulation. We will also study the sensitivity of the simulated MJO in the CAM2 to this downdrafts fraction.

Nordeng (1994) revised the closure condition of the Tiedtke (1989) scheme for deep or penetrative convection with other features being retained. Cloud base mass flux is determined by convective instability and the scheme is closed on CAPE. It is noteworthy that, in Nordeng (1994), the moisture convergence serves as a first estimate and is used to calculate updrafts and downdrafts and then determine the cloud base mass flux for deep convection. From this point of view, moisture convergence is still functioning in deep convection in this revised scheme. Sensitivity of the MJO in the CAM2 to the closure conditions will be discussed in subsequent sections.

The Zhang and McFarlane (1995) scheme is also a bulk model based on the mass flux concept, but it only parameterizes deep convection. It assumes that all clouds share the same cloud base where the mass flux solely depends on CAPE. Updrafts and downdrafts are considered for deep convection. The mass flux has an e-folding distribution in updrafts. Why this scheme produces an MJO with much lower amplitude both in thermo and dynamical fields in the tropical troposphere deserves further investigation. In this study, we will focus on the improvement of the MJO simulation over the Indian-Pacific Oceans where MJO convection is strongest in observations.

2.3. Experimental design and analysis procedure

We run the CAM2 with different convective schemes or the same scheme with different configurations of closure and downdrafts. Table 1 lists conventions for all the runs. The standard release of the CAM2.0.2 serves as a control run using the Zhang and McFarlane (1995) deep convective scheme and is named as CTL. Runs using the Tiedtke convective scheme are all represented by a capital letter T in the abbreviations with another capital letter N representing the Nordeng (1994). The double DD in the abbreviations represents downdrafts.

Sixteen-year long AMIP-type (Gates 1992) runs are conducted. Boundary conditions are observed time-evolving monthly mean sea surface temperature and sea ice provided by the CAM2 standard release. All runs cover January 1, 1978 to March 31, 1995, while outputs for analysis only cover January 1, 1979 to December 31, 1994. Monthly mean outputs are used for mean state analysis. Daily mean outputs in winds, surface latent heat flux, precipitation and moisture are used for the MJO diagnostics. Pentad (5-day) mean data are derived from the daily mean output. By subtracting their long-term means, daily and pentad anomaly series are derived. A

4-16 pentad (20-80 day) band pass filter is applied to the complete anomaly series without any tapering. Results here are in good agreement with previous studies where each season was separately windowed and tapered before filtering (e.g. Salby and Hendon 1994). November-April (about 180 days) anomaly series are used for an extended winter (winter in short). Power spectra and regression plots are then derived to analyze the modeled MJO features.

2.4. Observational data

Winds are from the National Centers for Environmental Prediction-National Center for Atmospheric Research (NCEP-NCAR) reanalysis project (Kalnay et al. 1996). We compare the simulated precipitation to the pentad averaged Climate Prediction Center Merged Analysis of Precipitation (CMAP; Xie and Arkin 1997) although MH98 indicated that the CMAP data shows somewhat stronger MJO amplitude than other sources. The same filtering procedure for the model output will be applied to the observational data.

3. Mean state and MJO in the CAM2 experiments

3.1 DJFM Mean State: 850hPa Zonal Wind and Precipitation

Since the mean states are important for MJO simulation, in this subsection, we show the mean states in 850 hPa zonal wind and precipitation during December-March season in the CTL, TN_DD30, and T_DD20 compared to the NCEP-NCAR reanalysis and CMAP rainfall.

Figure 1 shows long-term mean (1979-1994) 850 hPa zonal wind in the tropics for the DJFM season. In the reanalysis (Fig. 1a), westerly winds are located over the southern equatorial regions over Africa, the Indian and western Pacific Oceans and South America. From the Indian Ocean to central Pacific the westerlies correspond to the location where the eastward propagation of the MJO is prevalent. The CTL run (Fig. 1b) produces westerly winds over the Indian and western Pacific Oceans. Importantly, this westerly patch centers at 110^{o}E and only extends to 160^{o}E, suggesting that if eastward propagation of the MJO is present, it will not penetrate as far east as observed. The TN_DD30 simulation (Fig. 1c) fails to represent the westerlies over the tropical Indian Ocean, but better simulates their extension to the date line (also seen in the TDD_20) compared to the CTL run. The westerlies over the Indian Ocean are modestly improved in the T_DD20 simulation. Figure 1 indicates that the convective parameterization can greatly contribute to the mean state in 850 hPa zonal wind. The CAM2 with the Tiedtke (1989) scheme closed on moisture convergence with reduced downdrafts (T_DD20) produces a more realistic mean zonal wind than the Tiedtke scheme closed on static instability (TN_DD30), though compared to observations and the CTL run the westerlies over the Indian Ocean are deficient.

Figure 2 shows the mean state of precipitation in the DJFM season. Similar to CCM3, results from Maloney and Hartmann (2001) indicate the CTL run (Fig. 2b) produces much weaker than observed (Fig. 2a) precipitation over the south equatorial Indian and Pacific Oceans. Additionally, precipitation over the South Pacific Convergence Zone (SPCZ) is generally about half of that observed. Such a weak mean state in precipitation will be shown to correspond to a

much weaker MJO amplitude in these regions. Comparatively, the TN_DD30 (Fig. 2c) enhances the precipitation over the SPCZ region so that it is comparable to CMAP, and that over the Indian Ocean is also improved. The T_DD20 (Fig. 2d) produces a precipitation distribution that is closest to CMAP, particularly over the southern Indian and western Pacific Oceans. Despite the improvement over the Indian and Pacific Ocean in the simulations using the Tiedtke scheme, the rainfall over the Maritime continent remains underestimated compared to observations. The change of mean states can be understood in that tropical convections on different temporal and spatial scales are represented differently by different cumulus schemes. We next explore the relationship of the mean state to the intraseasonal variance.

3.2 Mean intraseasonal variance of precipitation

Figure 3 shows the 20-80 day bandpass filtered precipitation variance for the months November to April. CMAP has variance in excess of 20 mm^2/day^2 over the Indian and western Pacific Oceans, with a minimum over the Maritime continent (Fig. 3a), while the CTL simulation fails to produce variance of this magnitude (Fig. 3b). The runs with the variants of the Tiedtke scheme have more intraseasonal variability, with the T_DD20 overestimating the precipitation variance. When expressed as a percentage of the total variance, improvement using the Tiedtke schemes compared to the CTL scheme is also apparent (Fig. 4). Even so, compared to observations (Fig. 4a) the percent of total variance explained by 20-80 day periods is still underestimated in the Tiedtke sensitivity runs. In the case of T_DD20, both the bandpass filtered (Fig. 4d) and the total variance (not shown) are substantially overestimated compared to observations.

In summary, the CTL run produced MJO variance is much lower than observed in both precipitation and 850 hPa zonal wind (not shown). The Tiedtke scheme closed on CAPE with enhanced downdrafts, TN_DD30 has an improved climatology but deficiencies remain, particularly over the equatorial Indian Ocean. The scheme closed on moisture convergence and reduced downdrafts, T_DD20, produces a rainfall climatology closer to observations, but with much higher variance in the 20-80 day band for both precipitation (Fig. 3d) and 850hPa zonal wind (not shown).

3.3 Mean power spectra

The MJO variance shown in Fig. 3 may consist of standing and propagating components, which can be evaluated using wavenumber-frequency analysis. Fourier power spectra of 7^oN-7^oS averaged 850hPa zonal wind are calculated using the bandpass filtered series for each of the fifteen winters. The spectra are averaged to obtain the mean power spectrum. As shown in the observational studies (e.g. Hendon and Salby 1994), the MJO propagation dominates the 850 hPa zonal wind and is highly coherent with the convective fields. As seen in Fig. 5a, the observed mean power spectrum is dominated by eastward propagation at zonal wave numbers 0-3 and periods from 30 to 70 days. The little energy that propagates westward is dominated by wave numbers 0-2 at a period of 60 days. The power asymmetry in the direction of propagation indicates that eastward propagation dominates.

The CTL simulation (Fig. 5b) produces a weak power spectrum, consistent with those from CCM3 shown by Maloney and Hartmann (2001). The TN_DD30 (Fig. 5c) run has an improved power spectrum with eastward propagation that is much stronger than westward, and with maxima concentrated at zonal wave numbers 0-3 and periods of 20-70 days. However, the power in the TN_DD30 simulation is only about half the amplitude of the reanalysis. The T_DD20 (Fig. 5d) shows the best agreement with the reanalysis, though the eastward power has two maxima at 30 and 50 days. This deficiency was found to exist in many earlier AGCMs by Slingo et al. (1996).

Space-time power spectra of precipitation are shown in Fig. 6. The power spectrum from CMAP in Fig. 6a shows very similar features to that from the 850 hPa zonal wind except for a wider range of dominant zonal wave numbers. Figure 6b shows that the CTL run has very weak power and lacks dominant eastward propagation, similar to that in the zonal wind in Fig. 5b. Although the TN_DD30 simulation produces stronger MJO power spectra than the CTL in the zonal wind, it does not simulate a commensurate improvement for rainfall (Fig. 6c). The Tiedtke convective scheme closed on moisture convergence (T_DD20; Fig. 6d) produces a more coherent MJO-like power spectrum in precipitation than when closed on CAPE (TN_DD30, Fig. 6c). In the CAM2 framework, a convective scheme closed on static energy or CAPE does not show much advantage in simulating a realistic spectrum of MJO precipitation. This is possibly related to the poor zonal wind (Fig. 1c) and precipitation climatologies, and the weak intraseasonal variability over the Indian Ocean (Fig. 3c).

3.4 Regression with 850 hPa zonal wind

Here we use lagged linear regression to ascertain how well the various simulations represent intraseasonal eastward propagation of the near-equatorial 850 hPa zonal wind. This will enable us to isolate the sensitivity simulation in which a more in-depth analysis should be pursued. Following MH98, we select 155^{o}E as a reference point. Filtered time series are averaged between 10^{o}N and 10^{o}S in the reanalysis and CAM2 experiments. The latitudinal range for averaging is 3^{o} wider here than for the power spectra in Figs. 5 and 6 to extract a more continuous propagating signal in the reanalysis; only a slight difference occurs in the CAM2 runs when using 7^{o}N ~ 7^{o}S. In Fig. 7a the lead-lag correlation in northern winter from the reanalysis shows onset of the MJO in the Indian Ocean at time lags of -30 to -15 days. East of the dateline the signal propagates eastward with a faster phase speed relative to that in the Eastern Hemisphere. The period of the oscillation is about 45 days, consistent with the results of Woolnough et al (2000) and Sperber (2003). The CTL simulation shows virtually no propagating signal (Fig. 7b), consistent with the CAM2 analysis by Sperber (2004) and the CCM3 investigation of Maloney and Hartmann (2001). Figures 7c and 7d indicate that the variants of the Tiedtke scheme give rise to eastward propagating intraseasonal variability. That closed on moisture convergence, T_DD20 (Fig. 7d), gives an excellent representation of the variations of the phase speed across the tropics and has a realistic amplitude. However, the period is faster than observed, consistent with the space-time spectra in Fig. 5d. This is the simulation on which we concentrate our more in-depth analysis of the MJO given the well-defined eastward propagating signal.

4. The Composite Life Cycle of the Model MJO

An MJO index is derived similar to MH98. The filtered pentad anomalies are averaged from 7^oN to 7^oS for both model (T_DD20) and the reanalysis. Subsets are retrieved for the fifteen extended winters from 1979 to 1993. Intraseasonal variations in the 850hPa zonal wind are extracted using Empirical Orthogonal Function (EOF) analysis. EOF-1 and EOF-2 from the reanalysis and model are displayed in Fig. 8. In both model and reanalysis, the first two EOF's are significantly different from the higher order modes based on the criterion developed by North et al. (1982). The model (Fig. 8b) captures the quadrature relationship over the Eastern Hemisphere seen in the reanalysis (Fig. 8a). Model EOF-1 has a maximum over the Indian Ocean and a minimum over the Western Pacific Ocean, comparable to observations. The model EOF-2 peaks near 130^oE, slightly west of the reanalysis, and to the east the amplitude decreases faster than observed. Simulated EOF-1 (EOF-2) explains comparable (slightly less) variance than observed.

The quadrature relationship between the first two EOF's is further shown by the lag correlation coefficients of the corresponding principle components (PC's; Table 2). The simultaneous correlation coefficient is very close to zero in both model and reanalysis, thus exhibiting their orthogonality. From Table 2 we note that for the reanalysis the lag correlations for pentads 1-3 are similar, while in the model it drops dramatically at a lag of 3 pentads. This is consistent with the faster than observed EOF-2 amplitude decline near the dateline (Fig. 8b). Consequently, we define the MJO index time series as a linear combination of the PC1 and PC2. The index for the model is defined as:

$$\text{Index1}(t) = \text{PC1}(t) + [\text{PC2}(t + 1) + \text{PC2}(t + 2)]/2, \qquad (1.1)$$

and for the reanalysis as:

$$\text{Index2}(t) = \text{PC1}(t) + [\text{PC2}(t + 1) + \text{PC2}(t + 2) + \text{PC2}(t+3)]/3, \qquad (1.2)$$

where t is the time in pentads.

We consider 9 phases in the composite life cycle of the MJO, though only a few are shown for brevity. MJO events are composited when the index is greater than or equal to one standard deviation (STD in short) in the fifteen year time series. The first point that is below or equal to −STD is a candidate for phase 1. Starting from this point, if the index advances to +STD or above and then reverses back to −STD or below, an MJO event is defined with the starting point denoted as phase 1. The maximum positive departure of the index (+STD) is phase 5 and the second minima at or below −STD is phase 9. Phases 1, 5, and 9 have to be present for the sequence to be considered an MJO event. Other phases may be missed because the selected events have different dominant periods. If the index is within 0.3 x STD of zero during the growth (decay) of the event it is denoted as phase 3 (phase 7). The value 0.3 is used to include more samples for the transition phase. The main features are unchanged if a smaller value is used. For the intermediate phases (those other than 1, 5, and 9) our criterion used to define the life-cycle of MJO events is relaxed such that the index does not have to be strictly increasing or decreasing. In

such cases phase reversals of $|0.1| \times$ STD are allowed, but no more than two consecutive time points can oppose the growth or decay of the event for the intermediate phase to be defined. After a selected MJO event, the point for phase 9 is the starting point for another potential event. There are twenty selected events while the number for each phase are different. Student-t tests are conducted to test the difference of the anomalies from zero. Band-pass filtered winds, surface latent heat flux, convergence, and precipitation are composited for each phase. Vertically integrated water vapor from the surface to 850 hPa is also composited because it is a key component in the frictional moisture convergence mechanism (Wang and Rui 1990; MH98; Sperber 2003). These variables are retrieved for compositing from the filtered records including all seasons. It is noteworthy that there is no event selected that spans two different winters.

Phase 1 occurs after the onset of convection over the western equatorial Indian Ocean (Fig. 9a). The onset occurs in the presence of low-level easterly wind anomalies, and suppressed convection dominates the tropical western Pacific Ocean, consistent with the observations of Sperber (2003). The flow at 850 hPa and 200 hPa shows the model captures the baroclinic structure of the MJO. Convergence at 1000 hPa (Fig. 9b) and positive boundary moisture anomalies (Fig. 9c) support the convection over the western Indian Ocean. The near equatorial moisture anomalies and convergence also occur further eastward suggesting pre-conditioning of the atmosphere in advance of the deep convection.

During phase 3 the enhanced rainfall of ~8mm day^{-1} is located near 90^{o}E, though it is characterized by two off-equatorial maxima (Fig. 10a). West of the precipitation weak vortices are anti-cyclonic at 200 hPa and cyclonic at 850 hPa off the equator. These features resemble a Rossby wave response (e.g. Gill 1980) to the precipitation (Rui and Wang 1990). It is noticed that numerous small convective centers lie near the equator from the eastern Indian Ocean to the west Pacific. As seen in Figs. 10b and 10c, the low-level convergence and enhanced moisture are in-phase with the enhanced convection. The enhanced rainfall over the west Pacific is contrary to observations that indicate in situ suppressed convection to be prevalent (Sperber 2003).

During phase 4, positive near-equatorial rainfall anomalies extend from 90^{o}E-160^{o}E, and weak low-level convergence extends to the dateline (not shown). However, a commensurate increase in low-level moisture near the dateline is lacking. In phase 5 the equatorial rainfall extends to the dateline as suppressed convection takes hold over the western Indian Ocean (Fig. 11a). The Rossby-Kelvin wave structure in winds is clearly defined, and shifts eastward 60-80^{o} compared to phase 3 (Fig. 10a). Convergence at 1000 hPa and low-level positive moisture anomalies extend across the date line, leading the positive precipitation eastward.

During phases 6 (not shown) and 7 (Fig. 12a) the enhanced rainfall extends east of the dateline and it bifurcates. The Southern Hemisphere branch weakens as it migrates into the South Pacific Convergence Zone, and the Northern Hemisphere component, which is not typically seen in other observed studies, tends to be weaker with slight migration to the northeast.

As noted above, there are times when either, or both, the low-level convergence and enhanced moisture precede the subsequent development of convection, most notably during the transition

from phase 4 to phase 6. Longitude-phase plots of anomalies of 7^oN-7^oS averaged precipitation and 1000 hPa convergence (Fig. 13a) and low-level moisture (Fig. 13b) indicate that weak preconditioning of the simulated atmosphere is evident from 120^oE-180^oE. However, there is a major discrepancy in the model, with the strongest near-surface convergence anomalies occurring in phase with the convection, unlike observations in which the convergence anomalies are in quadrature with the convection (Sperber 2003). Thus, the simulated low-level moisture convergence is not as demonstrative as in observations.

Figure 14 indicates a systematic error in the zonal winds that was also evident in the phase composites, namely that in the model (Fig. 14b) easterly anomalies at the leading edge of the convection dominate the low-level inflow, contrary to observations. With the systematic error of mean easterlies over the near equatorial Indian Ocean (Fig. 1d) the easterly intraseasonal anomalies give rise to enhanced evaporation at and to the east of the convection over the Indian Ocean that persists in phases 1-4 (Fig. 15), contrary to observations. This suggests that over the Indian Ocean wind induced surface heat exchange (WISHE, Emanuel 1987, Neelin et al. 1987) dominates in the model. Over the west Pacific, the simulated latent heat flux is more consistent with observations in that convection is preceded (followed) by suppressed (enhanced) evaporation. However,hfv Acv\-[0p8i54rqwertfjm .;00334txc 54rcv 0020v the dominance of the low-level easterly inflow relative to the convection arises due to the weaker preconditioning of low-level moisture convergence in the model.

5. Sensitivity experiment

In this section, we first show the sensitivity of the simulated MJO to enhanced downdrafts. Enhanced downdrafts compensate for updrafts to a great extent, and function to enhance re-evaporation of precipitation back into the environment. Net latent heating can be suppressed and the MJO can be reduced. The downdrafts are enhanced and specified as 30% of equivalent updrafts (named as T_DD30) as opposed to T_DD20 in which downdrafts are 20%.

Figure 16 shows the power spectra of 850 hPa zonal wind and precipitation in wavenumber –frequency domain. In 850 hPa zonal wind (Figs. 16a and 16b), the MJO power spectra maxima are both concentrated at zonal wave number 0-3 with a period of 30-70 days. Eastward power is larger than westward. These basic features do not change much with the enhanced downdrafts. However, the enhanced downdrafts tend to produce an MJO that has more power in periods shorter than 30 days (Fig. 14b) and less power in periods longer than 45 days. The amplitude of the power spectra is somewhat reduced after the downdrafts are enhanced. Similar sensitivity also exists in precipitation (Figs. 16c and 16d) where the dominant periods are shorter with the downdraft enhancement. The regression of 850 hPa zonal wind (not shown) indicates that the eastward propagation is faster in the Pacific Ocean with enhanced downdrafts, which is in agreement with the shorter dominant period in power spectra (Fig. 16).

Another sensitivity run uses the perpetual March design with T_DD20 convection to partly repeat analyses performed by Maloney and Hartmann (2001) and Maloney (2002) using CCM3 with the relaxed Arakawa-Schubert (McRAS) scheme of Moorthi and Suarez (1992) modified by Sud and

Walker (1999). The integration is the equivalent of 18 years duration with solar insulation and boundary conditions fixed to March 15. The most striking difference between the AMIP run and the perpetual March run is the power spectra at periods of 40-60 days. In the perpetual run, power is reduced by 40~50% in both zonal wind and precipitation; and the dominant period is concentrated closer to 30 days, which is supported by lag regression (not shown). For 850 hPa wind the power spectrum maxima near 30 days in the perpetual March run is larger than in the AMIP run. This is in agreement with the observations that the MJO is the strongest during March (Maloney and Hartmann 2001). Coherence among the zonal wind and precipitation remain mostly unchanged in the perpetual March run.

A composite life cycle in the perpetual run is derived following the procedures introduced in section 4 (not shown). The perpetual run shares two deficiencies with the CCM3 with McRAS (Maloney 2002). One is the jump of the positive precipitation anomalies from the Indian Ocean to the western Pacific although the discontinuity is narrower than in CCM3 with McRAS. Another deficiency is that positive precipitation anomalies occur in the eastern tropical Pacific where easterlies dominate at 850 hPa in the mean state. These two deficiencies do not occur in the AMIP run with the T_DD20 as shown in Fig. 14b. Consequently, from a phenomenological perspective the perpetual March run does not simulate as realistic an MJO as the AMIP run simply due to limitations of the perpetual March experimental design, unrelated to the convective scheme.

6. Summaries and discussions

This study investigated the Madden-Julian Oscillation (MJO) simulated by the NCAR Community Atmosphere Model version 2 (CAM2) with different convective parameterization schemes and different configurations of the Tiedtke (1989) convective scheme. The standard CAM2 that retains a default deep convective parameterization scheme of Zhang and McFarlane (1995) simulates less realistic mean state precipitation over the tropical Eastern Hemisphere, and no evidence of eastward propagating intraseasonal variability in the tropics. This confirms the deficiencies noted by Sperber (2004), and those previously noted in the CCM3 (Maloney and Hartmann 2001, and Maloney 2002), which also used the Zhang and McFarlane convection. Although these deficiencies in the CCM3 can be markedly reduced by an alternate relaxed Arakawa-Schubert (McRAS) scheme of Moorthi and Suarez (1992) modified by Sud and Walker (1999), some weaknesses remain, particularly in the Indian Ocean where weaker zonal winds at 850 hPa and deficient precipitation associated with the MJO were simulated. These deficiencies can be attributed to the McRAS scheme and the perpetual March experiment design used in Maloney and Hartmann (2001).

To attempt to simulate a more realistic MJO especially over the Indian Ocean, we implemented the Tiedtke (1989) convective scheme in the CAM2. The Tiedtke scheme (T_DD20) is closed on moisture convergence, a key component in the frictional moisture convergence mechanism for the MJO. Nordeng (1994) revised the Tiedtke scheme for deep convection by changing its closure from moisture convergence to CAPE (TN_DD30), and simulations with this scheme have shown good ability to represent the Madden-Julian variability during winter (Sperber 2004, personal communication) and summer (Kemball-Cook et al 2002, Fu et al. 2003). It is noteworthy that in

Nordeng's version (TN-DD30) moisture convergence still serves as a first estimate for the CAPE calculation and from this point of view the moisture convergence is still functioning. Different from Maloney and Hartmann (2001), who designed a perpetual March run, we conducted a series of AMIP type runs from January 1978 to March 1995 with specified monthly mean sea surface temperature (SST) and sea ice as external forcing. Our results show that the standard release version of the CAM2 (CTL) produces less reasonable mean states than the CAM2 with the Tiedtke (1989) convective schemes compared to observations, particularly for precipitation. The Nordeng revised scheme (TN_DD30) enhances the simulated precipitation over the Indian-Pacific Oceans but the amplitude is still too low in the equatorial Indian Ocean. Precipitation from the Tiedtke scheme (T_DD20) is the closest to observations with more realistic amplitude.

Intraseasonal filtered precipitation shows similar advantages and deficiencies in the CAM2 runs as in the mean state. Generally, the T_DD20 simulates the best agreement in spatial distribution with the observations except it has somewhat larger amplitude. Coinciding with previous studies, the observational data show that the MJO has more eastward propagation than westward, and power concentrated in zonal wave numbers 1-3 for periods of 30-70 days. The CTL run does not represent these features. The TN_DD30 simulates an MJO with power in zonal wind only half that observed and very weak power in precipitation, indicating weak coherence among the dynamical and convective fields. The T_DD20 produces most of the observed features, especially over the western and central Pacific Ocean, with comparable amplitude to the observations except for the dominant period also has a maximum new 30 days during the winter. In the CAM2 model the comparison between the TN_DD30 and T_DD20 indicates that the Tiedtke convective scheme closed on moisture convergence produces a better MJO than the scheme closed on moist static energy, contrary to the suggestion of Slingo et al. (1996).

A composite life cycle of the simulated MJO shows a more regular structure in the Eastern Hemisphere and the frictional convergence mechanism is more apparent than in CAM2 and the CCM3 with McRAS convection. The MJO initializes in the western Pacific and moves slowly eastward. A forced Rossby-Kelvin wave structure is clearly displayed in dynamical fields that move eastward with the convection. Despite the pronounced improvement in tropical eastward intraseasonal variability, the model displays two mechanisms for maintaining eastward propagation. With the easterly bias over the Indian Ocean in the time mean state, low-level easterly intraseasonal anomalies give rise to increased evaporation with wind induced surface heat exchange modulating the propagation. Over the western and central Pacific Ocean low-level convergence and moisture anomalies lead convection by 1-2 pentads, enabling moisture preconditioning and static energy build up. However, these leading anomalies are weaker than observed, and contrary to observations the strongest anomalies are more closely in phase with the convection. As a consequence easterly anomalies tend to dominate the low-level inflow to the convection in the model. Similar to observations, the dynamical signal radiates eastward at a faster phase speed once the intraseasonal convection ceases near the dateline.

Sensitivity experiments show that enhancing the downdrafts significantly shifts the MJO to shorter periods and reduces the MJO power, but to a lesser extent than if the scheme is closed on CAPE. Other features of the MJO remain unchanged, which is in agreement with previous studies. A

perpetual March run partly repeats the deficiencies in the CCM3 with McRAS, indicating an AMIP-type run with seasonally varying boundary conditions is more appropriate.

In CAM2 the Tiedtke (1989) scheme closed on moisture convergence simulates a better MJO than when it is closed on CAPE, although the same advantage does not occur in the ECHAM4 model that includes the Nordeng closure (not shown). Consequently, it cannot be concluded that the moisture closure of the Tiedtke scheme is superior to the CAPE closure. Other moist and diabatic processes in the CAM2 model may also contribute to the improvement of the MJO simulation when the Tiedtke convective scheme is implemented, including the interaction of convection with the boundary layer scheme. The Zhang and McFarlane (1995) scheme produces a reasonable mean state particularly in 850 hPa zonal wind. Why the Zhang and McFarlane (1995) scheme does not produce a realistic MJO structure is an interesting issue that deserves further investigation. To understand the reason will further advance the understanding of MJO in the simulation.

Acknowledgements

This research was supported by US Agency 1 through grant No. 123-4567, by US Agency 2 through grant No. 000-0000, and by the Japan Agency for Marine-Earth Science and Technology (JAMSTEC) through its sponsorship of the International Pacific Research Center. We thank Dr. Erik Roeckner for providing the Tiedtke convective scheme included in the ECHAM4.6. We thank CDC for providing the NCEP-NCAR reanalysis data. K. R. Sperber was supported by the U.S. Department of Energy, Office of Science Climate Change Prediction Program, at the University of California Lawrence Livermore National Laboratory under contract W-7405-ENG-48. B. Wang and T. Li acknowledge the support from NSF Climate Dynamics Program ATM-0329531 and ONR Grant N000140310739.

References

Arakawa, A., and W. H. Schubert, 1974: Interaction of a cumulus cloud ensemble with the large-scale environment. Part. I. *J. Atmos. Sci.*, **31**, 674-701.

Bladé, I., and D. L. Hartmann, 1993: Tropical intraseasonal oscillations in a simple nonlinear model. *J. Atmos. Sci,* **50**, 2922–2939.

Chao, W. C., and L. Deng, 1998: Tropical intraseasonal oscillation, super cloud clusters, and cumulus convection schemes. Part II: 3D aquaplanet simulations. *J. Atmos. Sci.*, **55**, 690-709.

Chao, W. C, and S.-J. Lin, 1994: Tropical intraseasonal oscillation, super cloud clusters, and cumulus convection schemes. *J. Atmos. Sci.*, **51**, 1282-1297.

Emanuel, K. A., 1987: An air-sea interaction model of intraseasonal oscillation in the Tropics. *J. Atmos. Sci.*, **44**, 2324-2340.

Fu, X., B. Wang, T. Li, and J. P. McCreary, 2003: Coupling between northward-propagating, intraseasonal oscillations and sea surface temperature in the Indian Ocean. *J. Atmos. Sci*., **60**, 1733-1753.

Gates, W. L., 1992: AMIP: The Atmospheric Model Intercomparison Project. *Bull. Amer. Meteor. Soc.*, **73**, 1962–1970.

Gill, A. E., 1980: Some simple solutions for heat-induced tropical circulation. *Quart. J. Roy. Meteor. Soc.*, **106**, 447-462.

Gualdi, S., A. Navarra, and G. Tinarelli, 1999: The interannual variability of the Madden-Julian oscillation in an ensemble of GCM simulations. *Climate Dyn.*, **15**, 643-658.

Hack, J. J., 1994: Parameterization of moist convection in the National Center for Atmospheric Research Community Climate Model (CCM2). *J. Geophys. Res.*, **99**, 5551-5568.

Hendon, H. H., and B. Liebmann, 1990: The Intraseasonal (30–50 day) Oscillation of the Australian Summer Monsoon. *J. Atmos. Sci.*, **47**, 2909–2924.

Hendon, H. H., Salby, M. L. 1994: The Life Cycle of the Madden–Julian Oscillation. *J. Atmo. Sci.*, **51**, 2225–2237.

Hendon, H. H., 2000: Impact of air-sea coupling on the Madden-Julian oscillation in a general circulation model. *J. Atmos. Sci.*, **57**, 3939-3952.

Hu, Q., and D. A. Randall, 1994: Low-Frequency Oscillations in Radiative-Convective Systems. *J. Atmos. Sci.*, **51**, 1089–1099.

Inness, P. M., and D. Gregory, 1997: Aspects of the intraseasonal oscillation simulated by the Hadley Centre Atmosphere Model. *Clim. Dyn.*, **13**, 441-458.

Inness, P. M., and J. M. Slingo, 2003: Simulation of the Madden–Julian oscillation in a coupled general circulation model. Part I: comparison with observations and an atmosphere-only GCM. *J. Climate*, **16**, 345–364.

Inness, P. M., and Coauthors, 2003: Simulation of the Madden–Julian Oscillation in a coupled general circulation model. Part II: the role of the basic state. *J. Climate*, **16**, 365–382.

Jones, C., and B. C. Weare, 1996: The Role of Low-Level Moisture Convergence and Ocean Latent Heat Fluxes in the Madden and Julian Oscillation: An Observational Analysis Using ISCCP Data and ECMWF Analyses. *J. Climate*, **9**, 3086–3104.

Lee, M.-I., I.-S. Kang, and B. E. Mapes, 2003: Impacts of cumulus convection parameterization on aqua-planet AGCM simulations of tropical intraseasonal variability. *J. Meteorl. Soc. Japan*, **81**,

963-992.

Kalnay, E., and Coauthors, 1996: The NCEP/NCAR 40-Year Reanalysis Project. *Bull. Amer. Meteor. Soc.*, **77**, 437–471.

Kemball-Cook, S., B. Wang, and X. Fu, 2002: Simulation of the intraseasonal oscillation in ECHAM4-4 model: The impact of coupling with an ocean model. *J. Atmos., Sci*., **59**, 1433-1453.

Kiehl, J. T., and Coauthors, 1998: The National Center for Atmospheric Research Community Climate Model: CCM3. *J. Climate*, **11**, 1131–1150.

Kuo, H.-L., 1974: Further studies of the parameterization of the influence of cumulus convection on large-scale flow. *J. Atmos. Sci.*, **31**, 1232-1240.

Lau, K. M., and Coauthors, 1989: Dynamics of super cloud clusters, westerly wind bursts, 30-60 day oscillations and ENSO: A unified view. *J. Meteor. Soc. Japan*, **67**, 205-219.

Madden, R. A., and P. R. Julian, 1971: Detection of a 40–50 Day Oscillation in the Zonal Wind in the Tropical Pacific. *J. Atmos. Sci.*, **28**, 702–708.

Madden, R. A., and P. R. Julian, 1972: Description of Global-Scale Circulation Cells in the Tropics with a 40–50 Day Period. *J. Atmos. Sci.*, **29**, 1109–1123.

Madden, R. A., and P. R. Julian, 1994: Observations of the 40–50-Day Tropical Oscillation—A Review. *Mon. Wea. Rev.*, **122**, 814–837.

Maloney, E. D., and D. L. Hartmann, 1998: Frictional Moisture Convergence in a Composite Life Cycle of the Madden–Julian Oscillation. *J. Climate*, **11**, 2387–2403.

Maloney, E. D., and D. L. Hartmann, 2001: The Sensitivity of Intraseasonal Variability in the NCAR CCM3 to Changes in Convective Parameterization. *J. Climate*, **14**, 2015–2034.

Maloney, E. D. 2002: An Intraseasonal Oscillation Composite Life Cycle in the NCAR CCM3.6 with Modified Convection. *J. Climate*, **15**, 964–982.

Manabe, S., J. Smagorinsky, and R. F. Strickler, 1965: Simulated climatology of a general circulation model with a hydrological cycle. *Mon. Wea. Rev.*, **93**, 769-798.

Meehl, G. A, and Coauthors, 1996: Modulation of equatorial subseasonal convective episodes by tropical-extratropical interaction in the Indian and Pacific Ocean regions. *J. Geophys. Res.*, **101**, 15033-15049.

Meehl, G. A., and Coauthors, 2001: A conceptual framework for time and space scale interactions in the climate system. *Clim. Dyn.*, **17**, 753-775.

Moorthi, S., and M. J. Suarez, 1992: Relaxed Arakawa-Schubert: A Parameterization of Moist Convection for General Circulation Models. *Mon. Wea. Rev.,* **120**, 978–1002.

Neelin, J. D., I. M. Held, and K. H. Cook, 1987: Evaporation wind feedback and low-frequency variability in the tropical atmosphere. *J. Atmos. Sci.,* **44**, 2341-2348.

Nordeng , T. E., 1994: Extended versions of the convective parameterization scheme at ECMWF and their impact on the mean and transient activity of the model in the tropics. ECMWF Technical Memorandum, No. 206, 41pp.

North, G. R., and Coauthors, 1982: Sampling Errors in the Estimation of Empirical Orthogonal Functions. *Mon. Wea. Rev.,* **110**, 699–706.

Park, C. K., D. M. Straus, and K. M. Lau, 1990: An evaluation of the structure of tropical intraseasonal oscillations in three general circulation models. *J. Meteor. Soc. Japan,* **68**, 403-417.

Rasch, P. J., and J. E. Kristjánsson, 1998: A comparison of the CCM3 model climate using diagnosed and predicted condensate parameterizations, *J. Climate*, **11**, 1587--1614.

Raymond, D. J., and D. J. Torres, 1998: Fundamental Moist Modes of the Equatorial Troposphere. *J. Atmos. Sci.,* **55**, 1771–1790.

Roeckner, E., and Coauthors, 1996: The atmospheric general circulation model ECHAM-4: Model description and simulation of present-day climate. Max Planck Institute for Meteorology, report 218, 90pp.

Rui, H., and B. Wang, 1990: Development characteristics and dynamic structure of tropical intraseasonal convection anomalies. *J. Atmos. Sci.*, **47**, 357-379.

Salby, M. L., and H. H. Hendon, 1994: Intraseasonal behavior of clouds, temperature, and motion in the Tropics. *J. Atmos. Sci.*, **51**, 2207-2224.

Salby, M. L., R. R. Garcia, and H. H. Hendon, 1994: Planetary-Scale Circulations in the Presence of Climatological and Wave-Induced Heating. *J. Atmos. Sci.,* **51**, 2344–2367.

Seager, R., and S. E. Zebiak, 1995: Simulation of Tropical Climate with a Linear Primitive Equation Model. *J. Climate*, **8**, 2497–2520.

Sheng, J., 1995: The Madden-Julian oscillation in the Canadian Climate Centre general circulation model. *Clim. Dyn.,* **12**, 125-140.

Slingo, J. M., and Coauthors, 1996: Intraseasonal oscillation in 15 atmospheric general circulation models: Results from an AMIP diagnostic subproject. *Climate Dyn.,* **12**, 325-357.

Sperber, K. R., 2003: Propagation and the vertical structure of the Madden–Julian Oscillation. *Mon. Wea. Rev.*, **131**, 3018-3037.

Sperber, K. R., 2004: Madden-Julian variability in NCAR CAM2 and CCSM2. *Climate Dyn.*, in press.

Sud, Y. C., and G. K. Walker, 1999: Microphysics of Clouds with the Relaxed Arakawa–Schubert Scheme (McRAS). Part I: Design and Evaluation with GATE Phase III Data. *J. Atmos. Sci.*, **56**, 3196–3220.

Sundqvist, H., 1988: Parameterization of condensation and associated clouds in models for weather prediction and general circulation simulation, in Physically-based Modeling and Simulation of Climate and Climate Change, Vol. 1, edited by M. E. Schlesinger, 433-461, Kluwer Academic.

Tiedtke, M., 1989: A comprehensive mass flux scheme for cumulus parameterization in large-scale models. *Mon. Wea. Rev.*, **117**, 1779-1800.

Wang, B., 1988: Dynamics of tropical low-frequency waves: An analysis of the moist Kelvin wave. *J. Atmos. Sci.*, **45**, 774-788.

Wang, B., and H. Rui, 1990: Dynamics of the Coupled Moist Kelvin–Rossby Wave on an Equatorial β-Plane. *J. Atmos. Sci.*, **47**, 397–413.

Wang, W., and M. E. Schlesinger, 1999: The Dependence on Convection Parameterization of the Tropical Intraseasonal Oscillation Simulated by the UIUC 11-Layer Atmospheric GCM. *J. Climate*, **12**, 1423–1457.

Wang, B., and T. Li, 1994: Convective Interaction with Boundary-Layer Dynamics in the Development of a Tropical Intraseasonal System. *J. Atmos. Sci.*, **51**, 1386–1400.

Waliser, D. E., K. M. Lau, and J.-H. Kim, 1999: The influence of coupled sea surface temperatures on the Madden-Julian oscillation: A model perturbation experiment. *J. Atmos. Sci.*, **56**, 333-358.

Woolnough, S. J., J. M. Slingo, and B. J. Hoskins, 2000: The relationship between convection and sea surface temperature on intraseasonal timescales. *J. Climate*, **13**, 2086-2104.

Xie, P., and P. A. Arkin, 1997: Global Precipitation: A 17-Year Monthly Analysis Based on Gauge Observations, Satellite Estimates, and Numerical Model Outputs. *Bull. Amer. Meteor. Soc.*, **78**, 2539-2558.

Yanai, M., B. Chen, and W.-W. Tung, 2000: The Madden-Julian oscillation observed during the TOGA COARE IOP: global view. *J. Atmos. Sci.*, **57**, 2374-2396.

Zhang, G. J., and N. A. McFarlane, 1995: Sensitivity of climate simulations to the parameterization of cumulus convection in the Canadian Climate Centre general circulation model. *Atmos.-Ocean*, **33**, 407-446.

Zhang, M., and Coauthors, 2003: A modified formulation of fractional stratiform condensation rate in the NCAR community atmospheric model CAM2. *J. Geophys. Res.*, **108(D1)**.

Table 1 Conventions for the integrations using the CAM2 incorporated with different convective schemes

Abbreviations	Deep convective scheme	Shallow/middle convective scheme
CTL	Zhang and McFarlane (1995), closed on CAPE	Hack (1994), closed on CAPE
TN_DD30	Tiedtke (1989) revised by Nordeng (1994), moisture convergence as a first guess of CAPE and closed on CAPE, downdrafts are 30% equivalent updrafts	Tiedtke (1989), closed on moisture convergence
T_DD30	Tiedtke (1989), closed on moisture convergence, downdrafts are 30% equivalent updrafts	Tiedtke (1989), closed on moisture convergence
T_DD20	Tiedtke (1989), closed on moisture convergence, downdrafts are 20% equivalent updrafts	Tiedtke (1989), closed on moisture convergence

Table 2 Correlation coefficients of PC1 leading PC2 from 0 to 7 pentads during the extended winters in 1979-1993.

Lead	0	1	2	3	4	5	6	7
NCEP	-0.000024	0.306	0.432	0.366	0.190	-0.003	-0.139	-0.175
T_DD20	0.0000200	0.530	0.530	0.156	-0.157	-0.227	-0.162	-0.073
DOF	538	537	536	535	534	533	532	531
99%	0.111							0.1117

Figure captions:

Fig. 1 Long-term (1979-1994) mean tropical 850 hPa zonal wind in December-March (DJFM) season. (a)-(d) are from the NCEP-NCAR reanalysis, CTL, TN_DD30, and T_DD20, respectively. Contour interval is 2 m/s excluding zero. Regions greater than and equal to zero are shaded.

Fig. 2 Long-term (1979-1994) mean tropical precipitation in December-March (DJFM) season. (a)-(d) are from the CMAP, CTL, TN_DD30, and T_DD20, respectively. Contour interval is 3 mm/day. Regions greater than and equal to 6 mm/day are shaded.

Fig. 3 Mean variance of 20-80 day filtered precipitation in extended winter (180 days from November to April). (a)-(d) are from the CMAP, CTL, TN_DD30, and T_DD20, respectively. Contour starts from 40 mm^2/day^2 with an interval of 20 mm^2/day^2. Regions greater than and equal to 20 mm^2/day^2 are shaded.

Fig. 4 Mean percentage of 20-80 day filtered to total variance of precipitation in winter. (a)-(d) are from the CMAP, CTL, TN_DD30, and T_DD20, respectively. Filtered variances equal to and less than 5 mm^2/day^2 are omitted.

Fig. 5 Mean wavenumber-frequency power spectra in 850 hPa zonal wind in winter. For each season from 1979 to 1994, power spectra are derived from the Fourier coefficients of filtered complete pentad time series averaged between 7^oS and 7^oN. An average of 15 seasons is derived. (a)-(d) are from the NCEP-NCAR reanalysis, CTL, TN_DD30, and T_DD20, respectively. Contour interval is 2.5 $m^2s^{-2}day$. Regions greater than and equal to 10 $m^2s^{-2}day$ are shaded.

Fig. 6 Mean wavenumber-frequency power spectra in precipitation using the same procedure as in figure 5. (a)-(d) are from the CMAP, CTL, TN_DD30, and T_DD20, respectively. Contour interval is 1 mm^2/day. Regions greater than and equal to 5 mm^2/day are shaded.

Fig. 7 Average lag correlation coefficients with filtered daily 850 hPa zonal wind in winter averaged $10^oS \sim 10^oN$ around the equator. (a)-(d) are from the NCAP-NCEP reanalysis, CTL, TN_DD30, and T_DD20, respectively. Contour interval is 0.2 m/s excluding zero. Regions greater than and equal to 0.2 m/s are shaded.

Fig. 8 Spatial distributions of the EOF1 (solid) and EOF2 (dashed) calculated from the filtered pentad 850 hPa zonal wind series during the extended winters from 1979 to 1993 (540 pentads in total) around the equator averaged between 7^oN and 7^oS in the NCEP-NCAR reanalysis (a) and the T_DD20 (b).

Fig. 9 Phase 1 of the composite life cycle of the MJO from T_DD20 with filtered anomalies during winter. (a) 200 hPa wind and precipitation. Interval for precipitation is 2 mm/day. (b) 850 hPa wind and 1000 hPa convergence (solid). Interval for convergence is 7×10^{-7} s^{-1}. (c) 1000-850 hPa integrated water vapor with interval of 0.5 g/Kg. Shaded and black vectors are values over a 90% confidence level of a Student-t test. All contour plots exclude zero. See text for the MJO

index and definitions for the phases.

Fig. 10 Same as Fig. 9 but for phase 3.

Fig. 11 Same as Fig. 9 but for phase 5.

Fig. 12 Same as Fig. 9 but for phase 7.

Fig. 13 Quadrature relationship of convection with 1000 hPa convergence (a) and 1000-850 hPa integrated moisture (b) during the composite life cycle of the MJO in T_DD20 based on the index in (1.1). Precipitation is color shaded with an interval of 1 mm/day excluding 0. Contour unit for convergence is 1×10^{-7} s^{-1} with levels of –20, -15, -10, -5, -1, 10, 15 and 20 shown. Unit for moisture is 1 g/kg with levels of –1.5, -1.2, -0.9, -0.6, 0.2, 0.6, 0.9, 1.2, and 1.5 shown.

Fig. 14 Convection and 850 hPa zonal wind averaged in 7^oN~7^oS in a composite life cycle of the MJO in observation (a; NCEP wind and CMAP rainfall) and T_DD20 (b) based on the indices in (1.1) and (1.2). Precipitation below –0.5 mm/day and above 0.5 mm/day is shaded with dark as positive and light as negative. Contour represents wind with solid as westerlies and dashed as easterlies. Interval for winds is 0.5 m/s.

Fig. 15 Same as figure 13 but contour for surface latent heat flux anomalies with interval of 5 W/m^2 starting from ±5. Positive anomalies correspond to oceanic cooling.

Fig. 16 Mean wavenumber-frequency power spectra in 850 hPa zonal wind (a and b) and precipitation (c and d) averaged in 7^oN~7^oS. (a) and (c) are from the T_DD20; (b) and (d) are from the T_DD30. Contour interval is 2.5 m^2s^{-2}day for (a) and (b), 1 mm^2/day for (c) and (d). Regions are shaded with greater than and equal to 10 m^2s^{-2}day in (a) and (b) and 5 mm^2/day in (c) and (d).

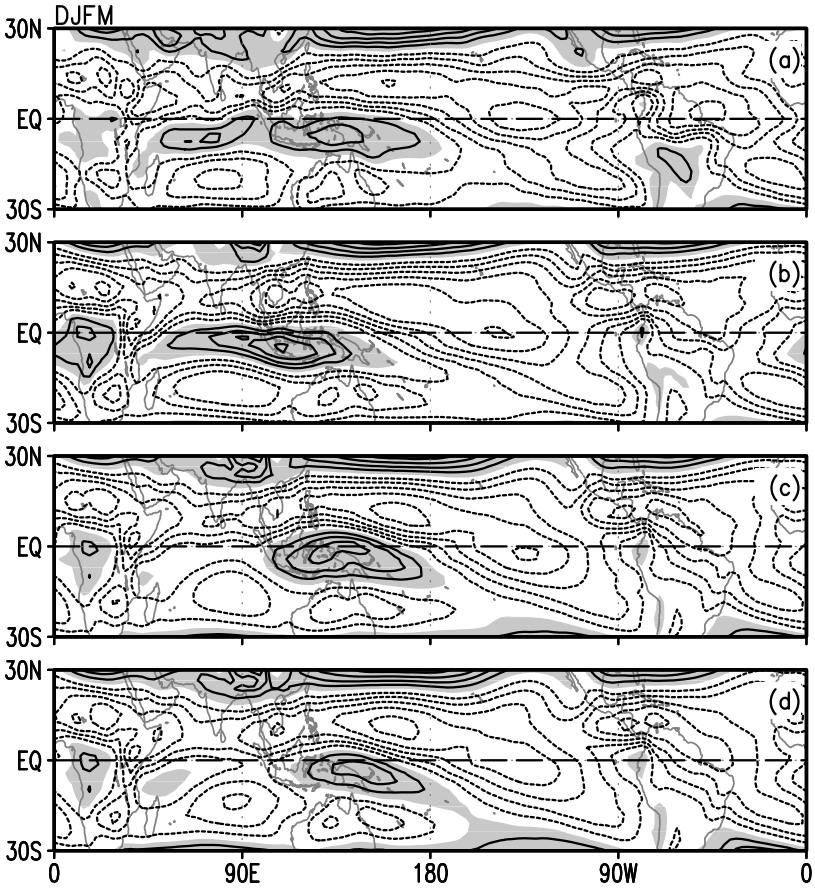

850 hPa u

(a) NCEP (b) CTL (c) TN_DD30 (d) T_DD20

isoline interval 2 m/s, 0 excluded; >= 0 m/s shaded

Figure 1

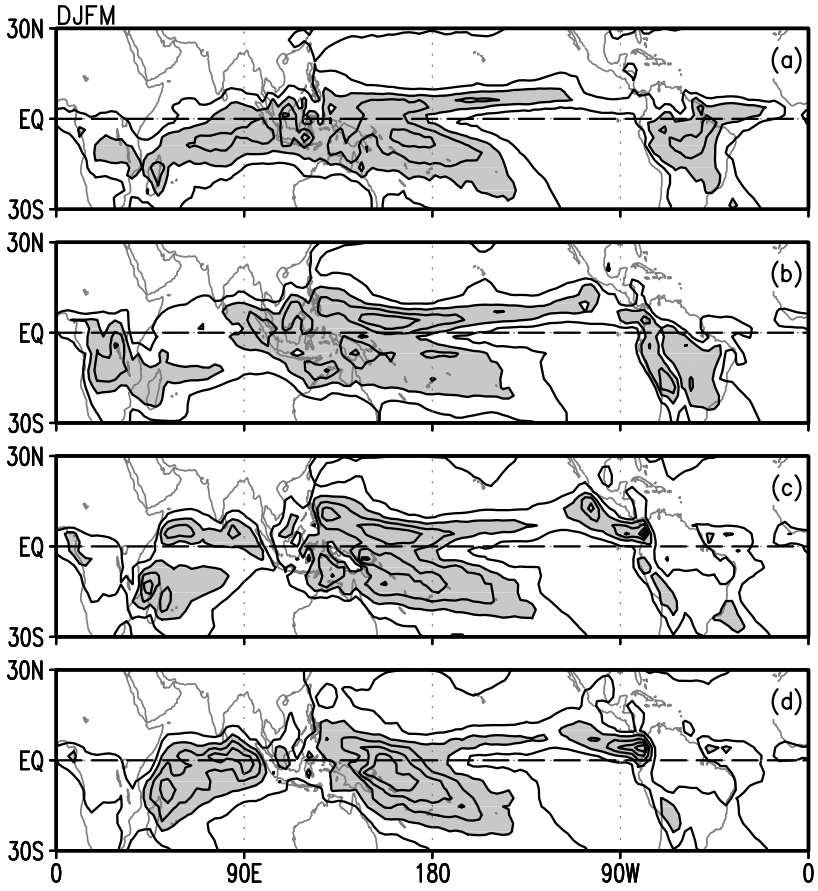

(a) CMAP (b) CTL (c) TN_DD30 (d) T_DD20
isoline interval 3 mm/day, >= 6 mm/day shaded

Figure 2

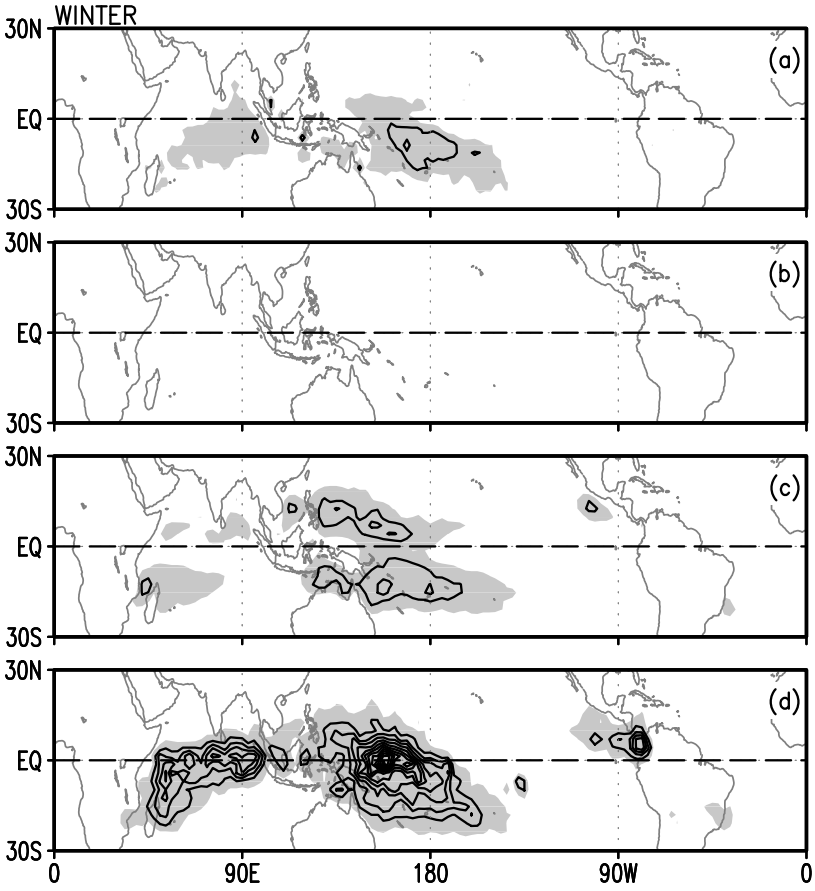

precipitation variance, see text for the definitions of WIN and SUM
(a) CMAP (b) CTL (c) TN_DD30 (d) T_DD20
isoline starts from 40 mm^2/day^2; shaded from 20 mm^2/day^2
interval 20 mm^2/day^2

Figure 3

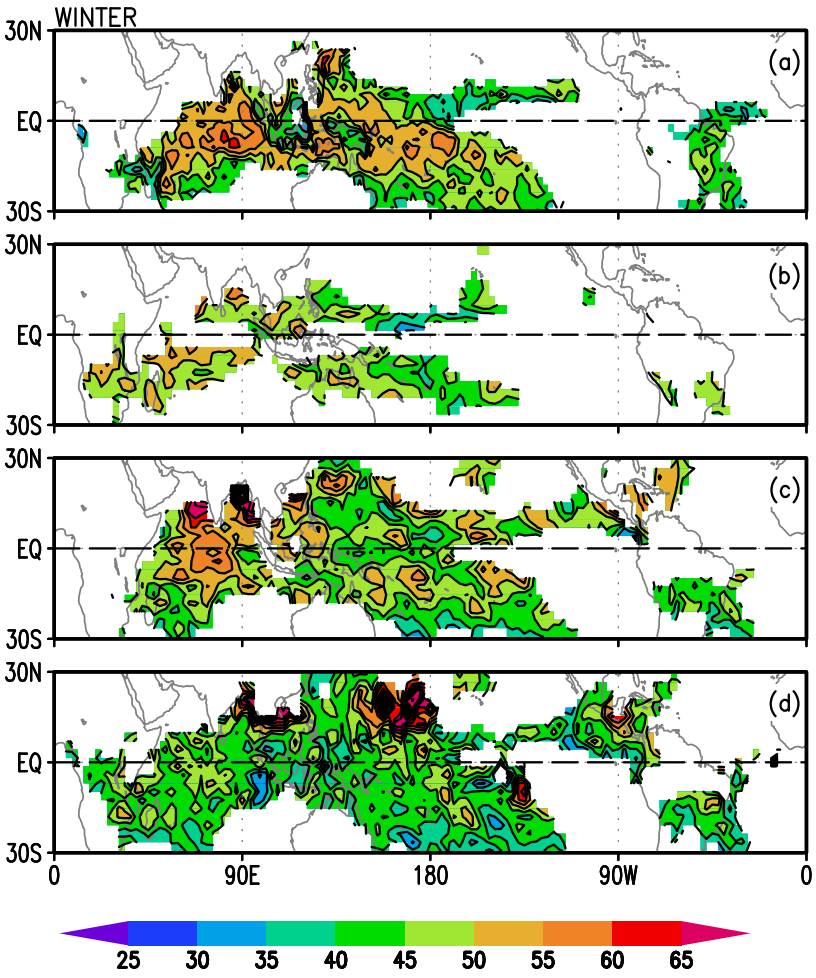

precipitation variance percentage (filtered MJO/total)
MJO variance <= 5 mm^2/day^2 are omitted, interval: 5
(a) CMAP, (b) CTL, (c) TN_DD30 (d) T_DD20

Figure 4

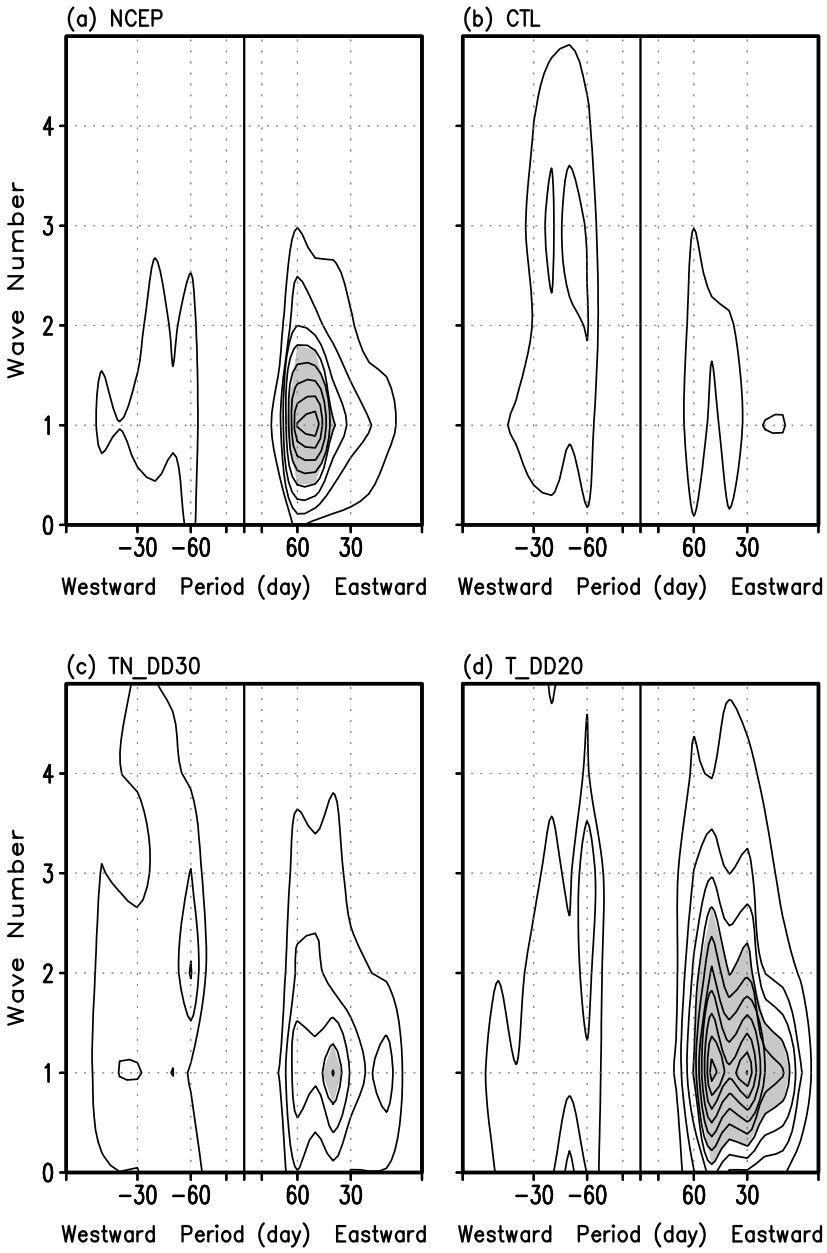
(a) NCEP
(b) CTL
(c) TN_DD30
(d) T_DD20
Wave Number
0
1
2
3
4
-30 -60
60 30
Westward Period (day) Eastward

Figure 5

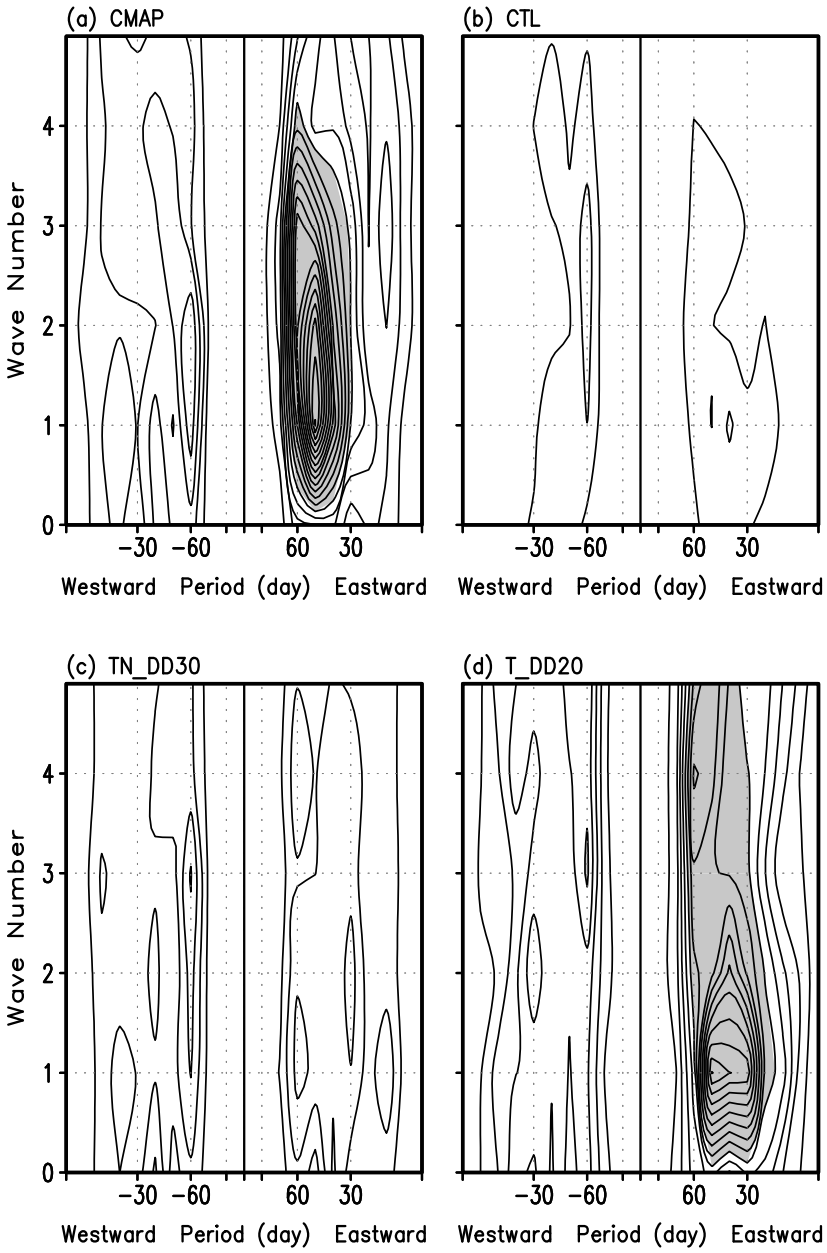
(a) CMAP
(b) CTL
(c) TN_DD30
(d) T_DD20
Wave Number
0
1
2
3
4
-30
-60
60
30
Westward
Period (day)
Eastward

Figure 6

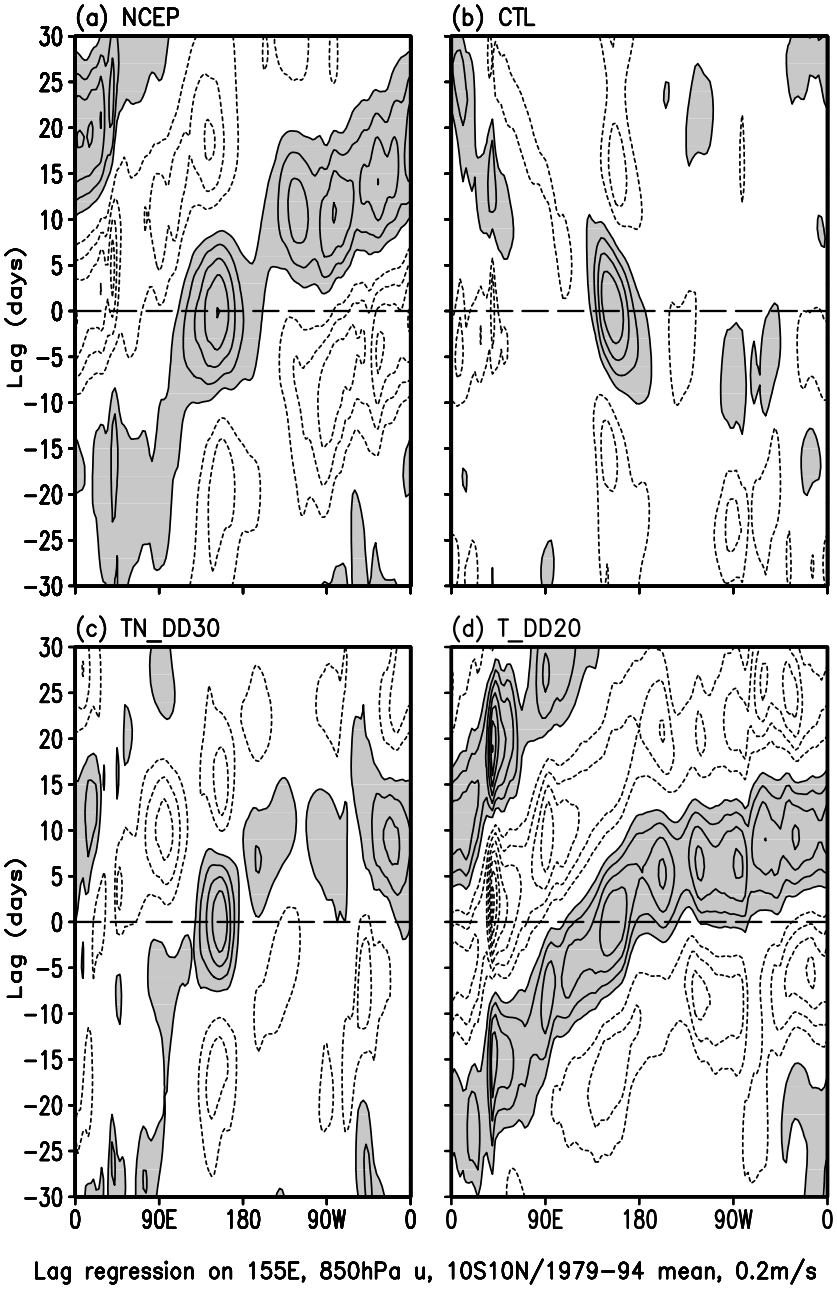
(a) NCEP
(b) CTL
(c) TN_DD30
(d) T_DD20
Lag (days)
30
25
20
15
10
5
0
-5
-10
-15
-20
-25
-30
0
90E
180
90W
0
Lag regression on 155E, 850hPa u, 10S10N/1979-94 mean, 0.2m/s

Figure 7

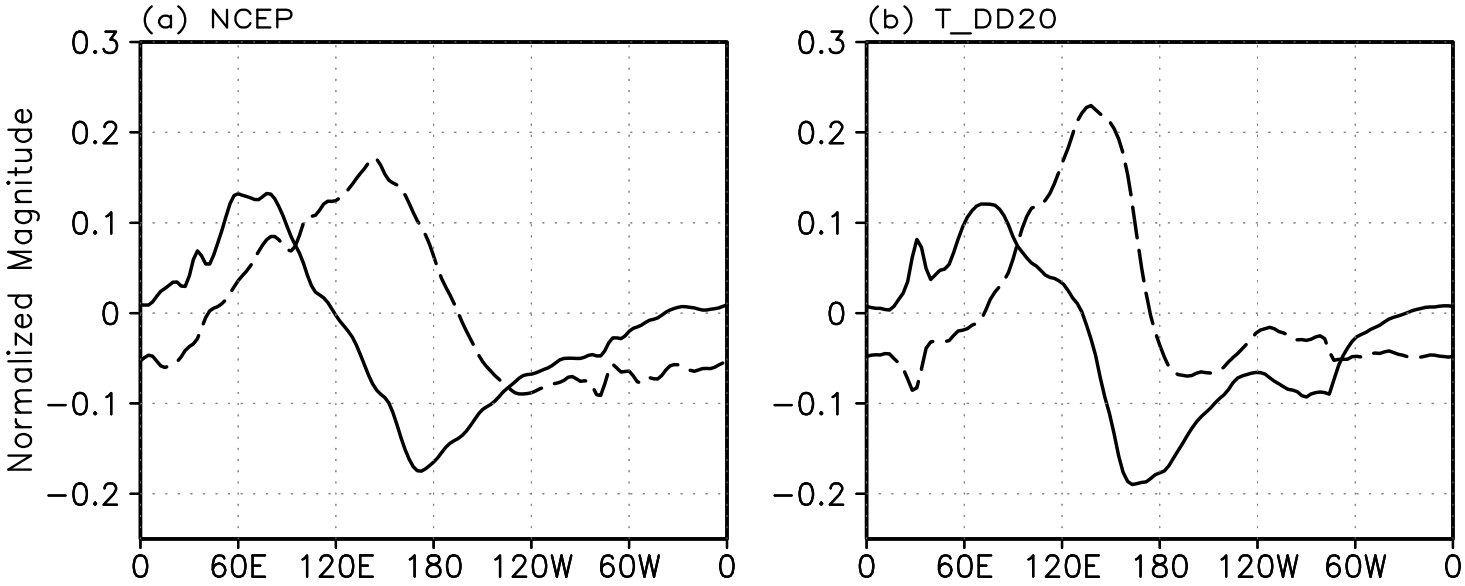

MH98 MJO indices (pentad anomaly 20−80 day band pass filtered) first two EOFs
Extended winters (Nov.2 ~ Apr.26), 1979~1993. EOF1: solid; EOF2: dashed
Explanation variance: (a) EOF1: 31.9%; EOF2: 23.1%
(b) EOF1: 29.4%; EOF2: 18.3%

Figure 8

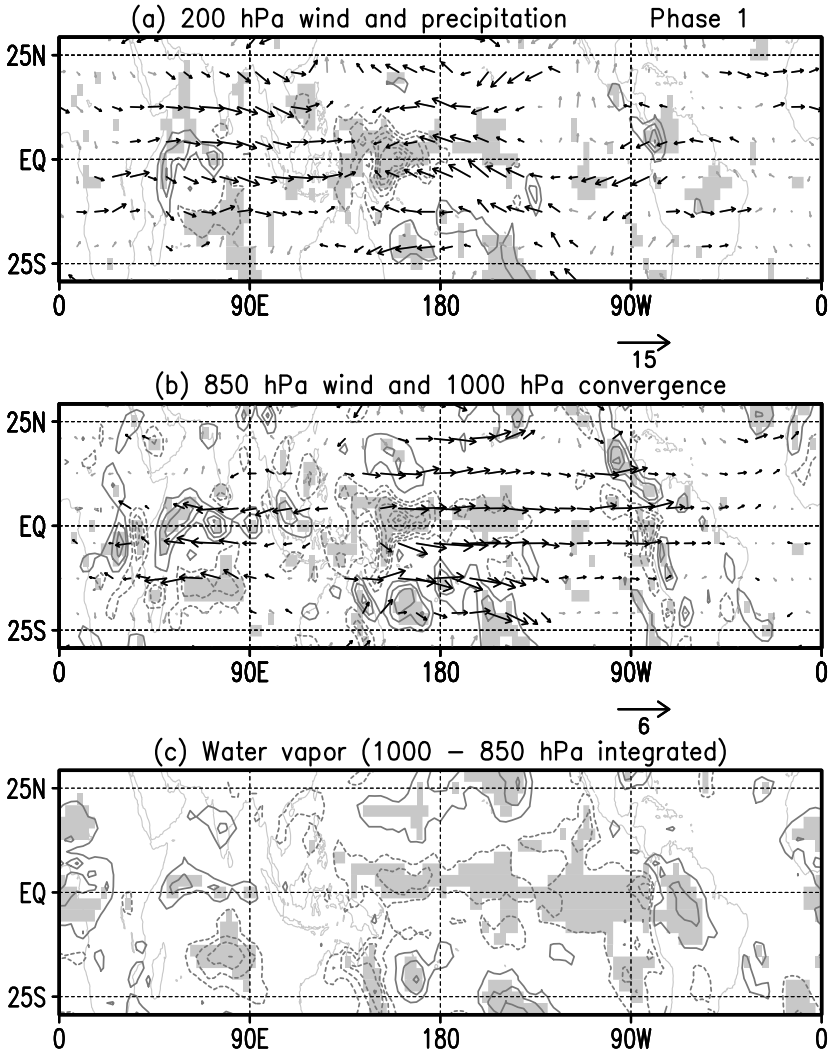
(a) 200 hPa wind and precipitation
Phase 1
25N
EQ
25S
0
90E
180
90W
0
15
(b) 850 hPa wind and 1000 hPa convergence
25N
EQ
25S
0
90E
180
90W
0
6
(c) Water vapor (1000 – 850 hPa integrated)
25N
EQ
25S
0
90E
180
90W
0

Figure 9

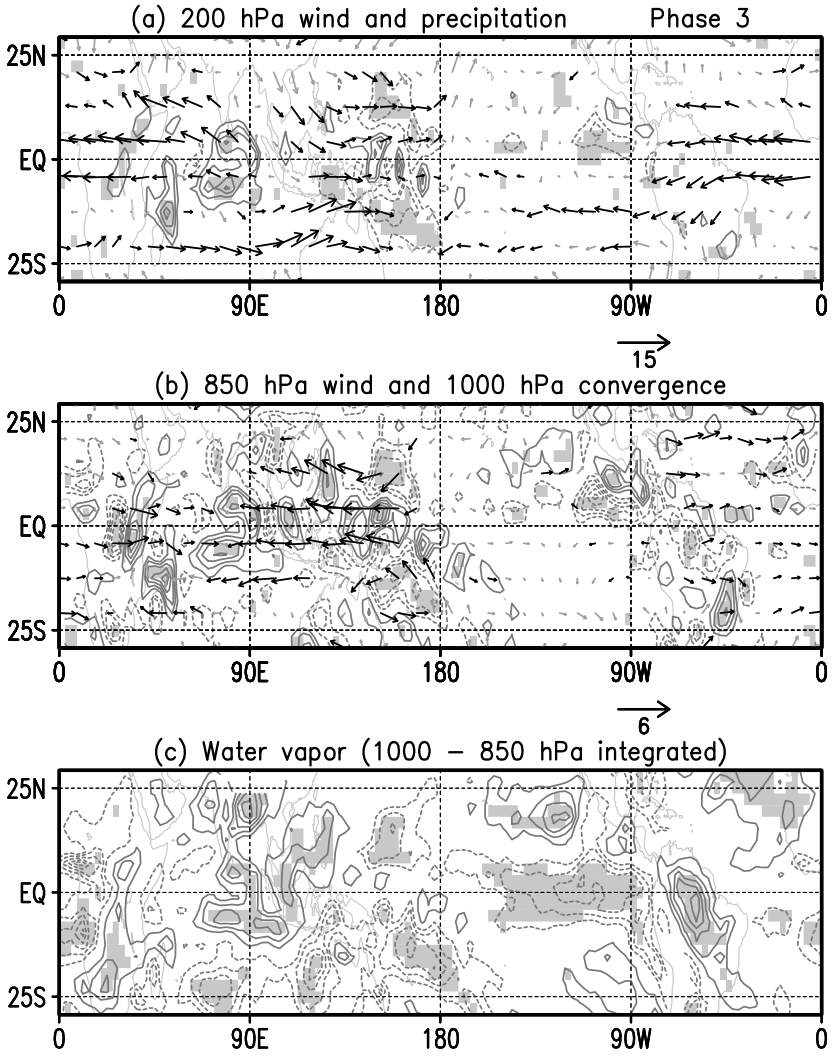
(a) 200 hPa wind and precipitation
Phase 3
25N
EQ
25S
0
90E
180
90W
0
15
(b) 850 hPa wind and 1000 hPa convergence
25N
EQ
25S
0
90E
180
90W
0
6
(c) Water vapor (1000 – 850 hPa integrated)
25N
EQ
25S
0
90E
180
90W
0

Figure 10

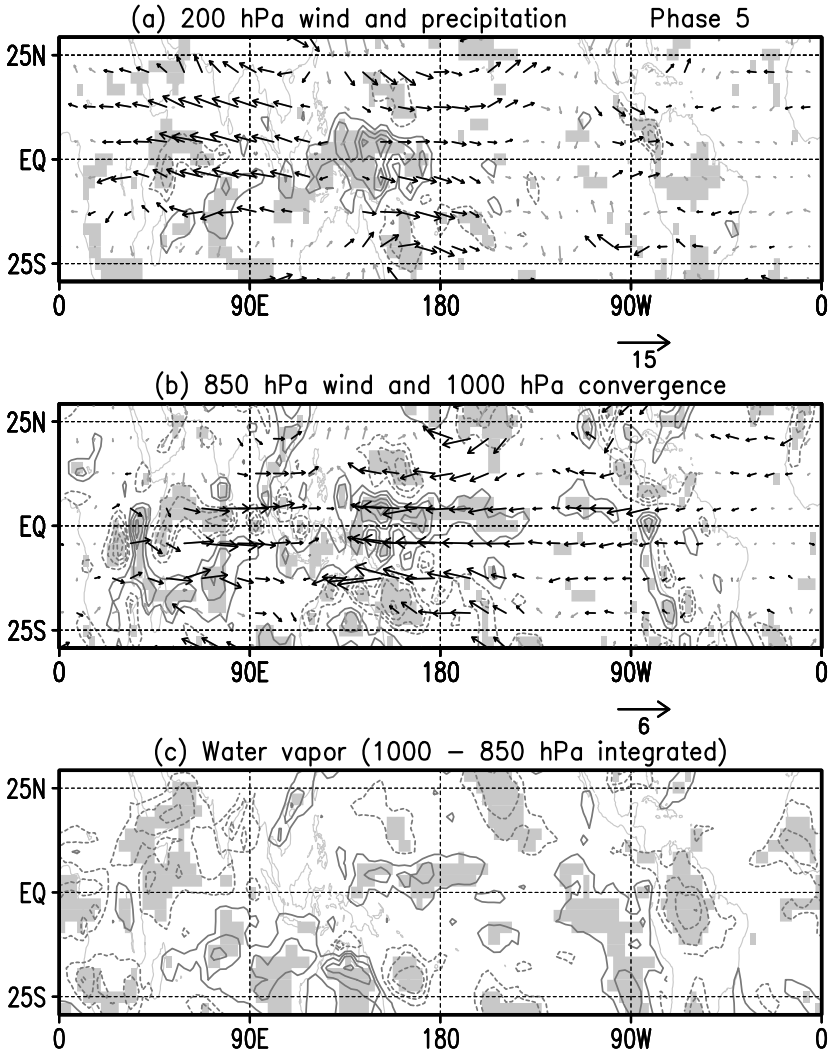
(a) 200 hPa wind and precipitation
Phase 5
25N
EQ
25S
0
90E
180
90W
0
15
(b) 850 hPa wind and 1000 hPa convergence
25N
EQ
25S
0
90E
180
90W
0
6
(c) Water vapor (1000 – 850 hPa integrated)
25N
EQ
25S
0
90E
180
90W
0

Figure 11

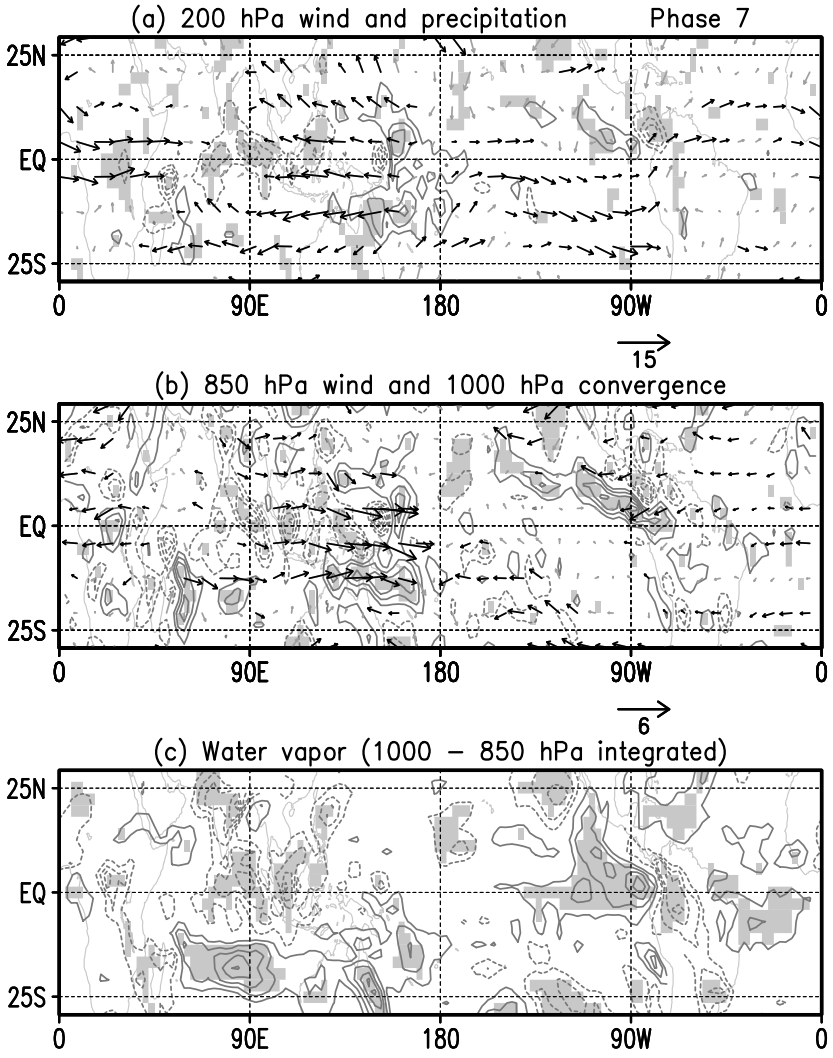
(a) 200 hPa wind and precipitation
Phase 7
25N
EQ
25S
0
90E
180
90W
0
15
(b) 850 hPa wind and 1000 hPa convergence
25N
EQ
25S
0
90E
180
90W
0
6
(c) Water vapor (1000 – 850 hPa integrated)
25N
EQ
25S
0
90E
180
90W
0

Figure 12

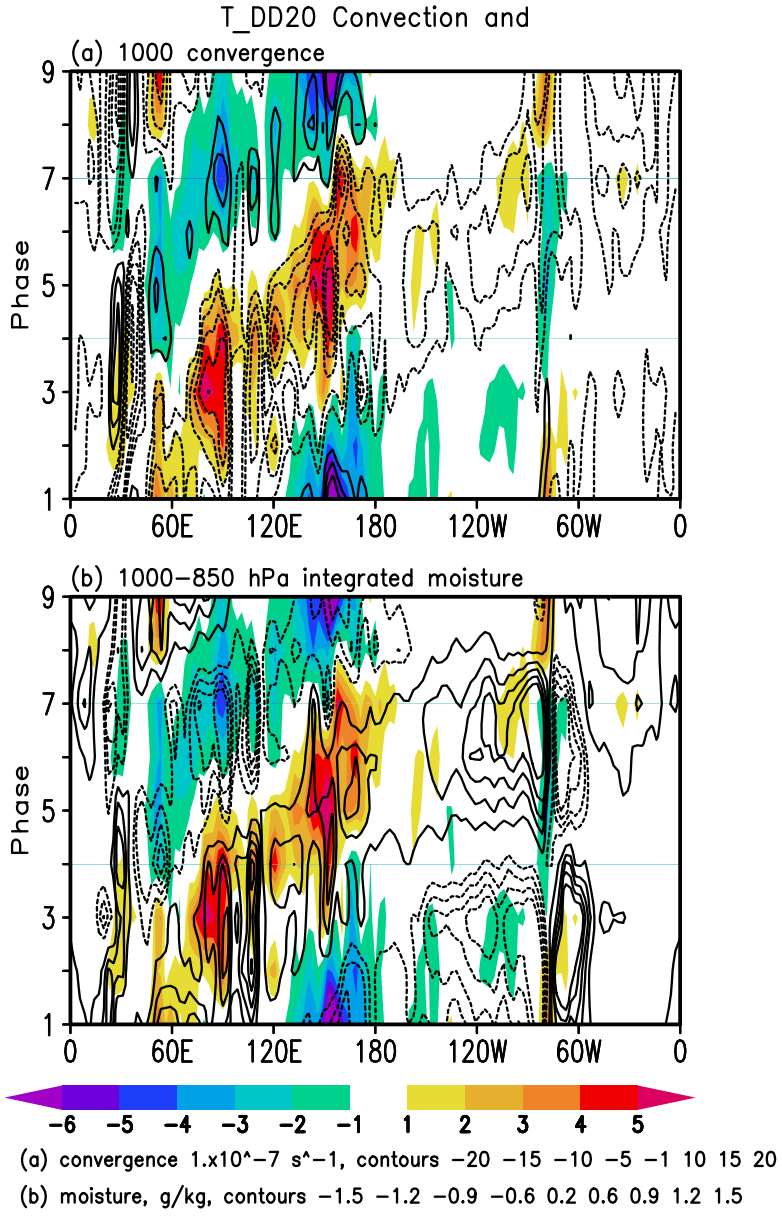
T_DD20 Convection and
(a) 1000 convergence
Phase
9
7
5
3
1
0
60E
120E
180
120W
60W
0
(b) 1000–850 hPa integrated moisture
Phase
9
7
5
3
1
0
60E
120E
180
120W
60W
0
−6 −5 −4 −3 −2 −1 1 2 3 4 5
(a) convergence 1.x10^−7 s^−1, contours −20 −15 −10 −5 −1 10 15 20
(b) moisture, g/kg, contours −1.5 −1.2 −0.9 −0.6 0.2 0.6 0.9 1.2 1.5

Figure 13

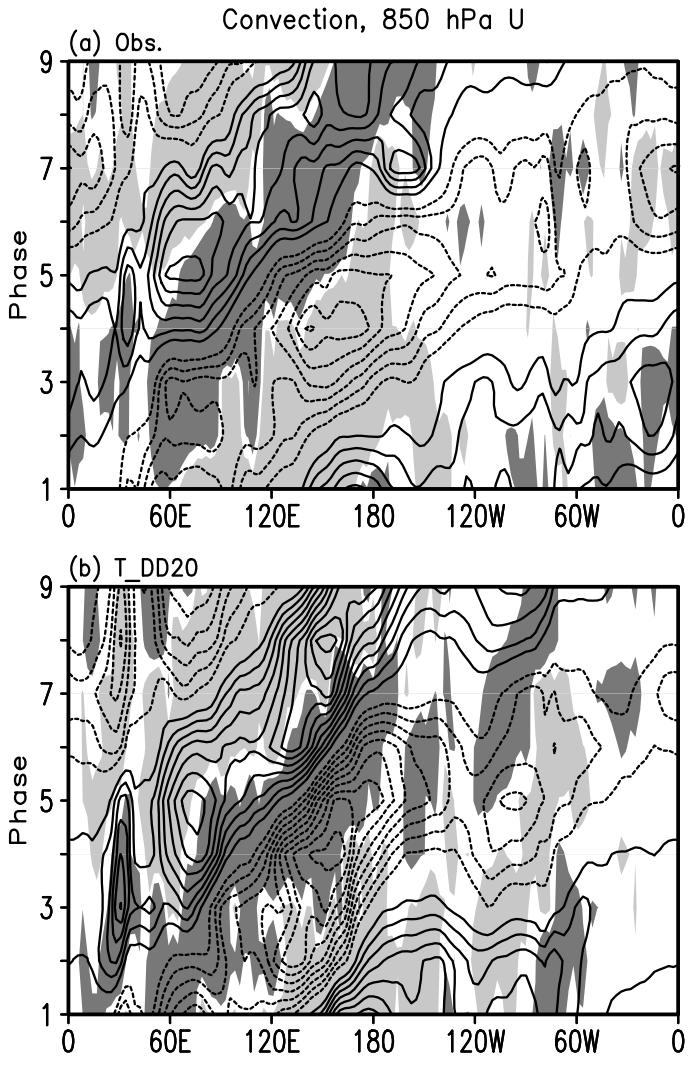
Convection, 850 hPa U
(a) Obs.
(b) T_DD20
Phase
9
7
5
3
1
0
60E
120E
180
120W
60W
0

Figure 14

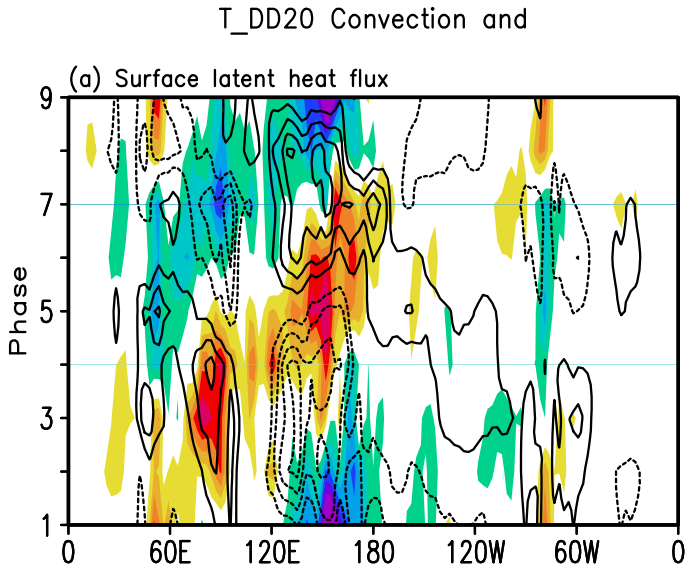

(a) Latent heat flux, W/m^2, contours 5, starting from +−5

Figure 15

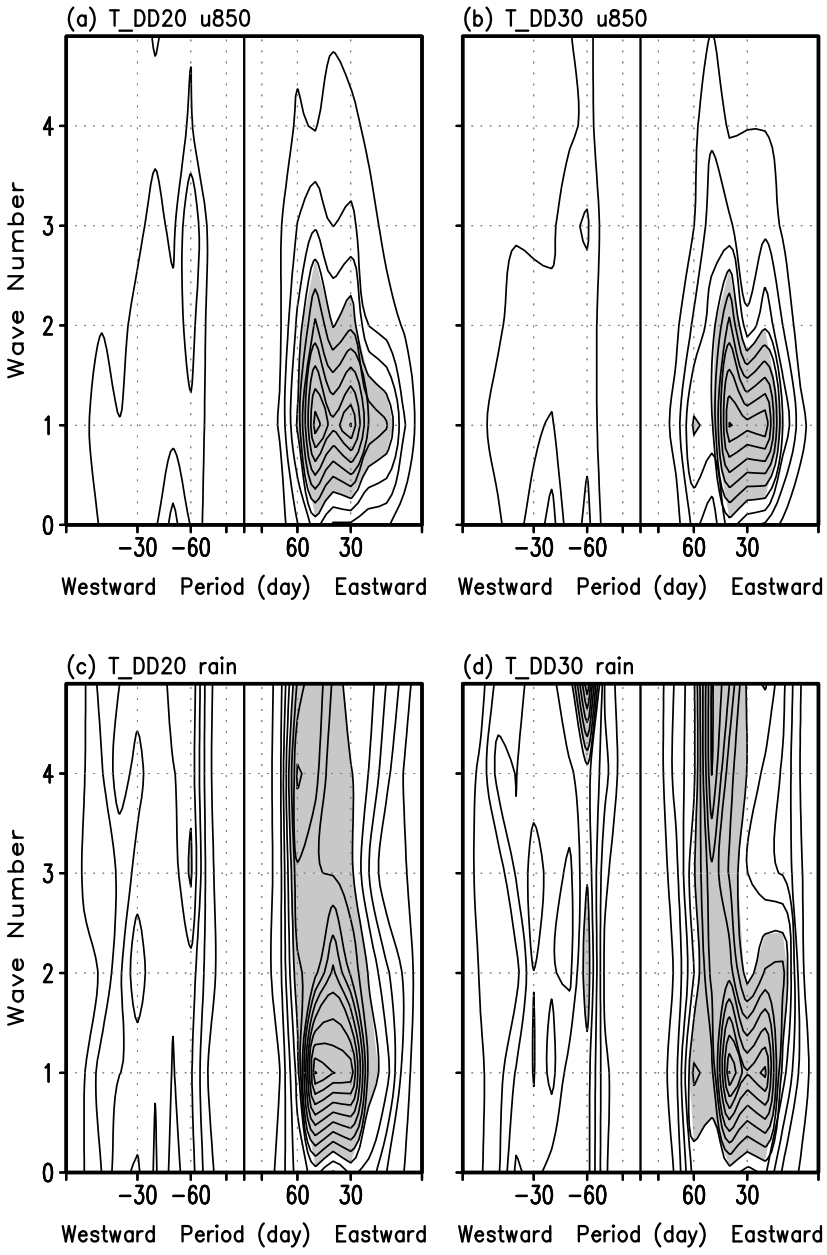
(a) T_DD20 u850
(b) T_DD30 u850
(c) T_DD20 rain
(d) T_DD30 rain
Wave Number
0
1
2
3
4
-30 -60
60 30
Westward Period (day) Eastward

Figure 16